# Natural Variability in a Stable, 1000-Yr Global Coupled Climate–Carbon Cycle Simulation

Scott C. Doney

*Marine Chemistry and Geochemistry, Woods Hole Oceanographic Institution, Woods Hole, Massachusetts*

Keith Lindsay

*Climate and Global Dynamics, National Center for Atmospheric Research,\* Boulder, Colorado*

Inez Fung and Jasmin John

*Berkeley Atmospheric Sciences Center, University of California, Berkeley, Berkeley, California*

### ABSTRACT

A new 3D global coupled carbon–climate model is presented in the framework of the Community Climate System Model (CSM-1.4). The biogeochemical module includes explicit land water–carbon coupling, dynamic carbon allocation to leaf, root, and wood, prognostic leaf phenology, multiple soil and detrital carbon pools, oceanic iron limitation, a full ocean iron cycle, and 3D atmospheric $CO_2$ transport. A sequential spinup strategy is utilized to minimize the coupling shock and drifts in land and ocean carbon inventories. A stable, 1000-yr control simulation [global annual mean surface temperature $\pm0.10$ K and atmospheric $CO_2 \pm 1.2$ ppm ($1\sigma$)] is presented with no flux adjustment in either physics or biogeochemistry. The control simulation compares reasonably well against observations for key annual mean and seasonal carbon cycle metrics; regional biases in coupled model physics, however, propagate clearly into biogeochemical error patterns. Simulated interannual-to-centennial variability in atmospheric $CO_2$ is dominated by terrestrial carbon flux variability, $\pm0.69$ Pg C $yr^{-1}$ ($1\sigma$ global net annual mean), which in turn reflects primarily regional changes in net primary production modulated by moisture stress. Power spectra of global $CO_2$ fluxes are white on time scales beyond a few years, and thus most of the variance is concentrated at high frequencies (time scale $<4$ yr). Model variability in air–sea $CO_2$ fluxes, $\pm0.10$ Pg C $yr^{-1}$ ($1\sigma$ global annual mean), is generated by variability in sea surface temperature, wind speed, export production, and mixing/upwelling. At low frequencies (time scale $>20$ yr), global net ocean $CO_2$ flux is strongly anticorrelated (0.7–0.95) with the net $CO_2$ flux from land; the ocean tends to damp (20%–25%) slow variations in atmospheric $CO_2$ generated by the terrestrial biosphere. The intrinsic, unforced natural variability in land and ocean carbon storage is the "noise" that complicates the detection and mechanistic attribution of contemporary anthropogenic carbon sinks.

---

## 1. Introduction

Over the last two centuries, the levels of atmospheric carbon dioxide ($CO_2$), an important greenhouse gas that modulates earth's radiative balance and climate,

*Corresponding author address:* Dr. Scott C. Doney, Marine Chemistry and Geochemistry, Woods Hole Oceanographic Institution, Woods Hole, MA 02543.
E-mail: sdoney@whoi.edu

have increased due to fossil fuel combustion and land use. Levels have risen from a preindustrial value of 280 ppm to about 380 ppm at present, equivalent to an increase of ~200 Pg of carbon (1 Pg = $10^{15}$ g; Prentice et al. 2001). By comparison, atmospheric carbon dioxide levels for the preceding several millennia of the Holocene were essentially flat, within $\pm5$ ppm of the preindustrial value. "Business as usual" economic and climate scenarios project values as high as 700–1000 ppm by the end of the twenty-first century, levels not experienced on earth for the past several million years (Pearson and Palmer 2000). There is growing evidence that this increase in atmospheric $CO_2$ will have a sig-

nificant, long-term impact on the planet's climate and biota (Houghton et al. 2001).

Recent estimates suggest that only about half of the fossil fuel $CO_2$ released by human activity during the last two decades has remained in the atmosphere; on average, about equal amounts or roughly 2 Pg C yr$^{-1}$ have been taken up by the ocean and land, respectively. As global climate models are improved, the future behavior of these land and ocean carbon sinks and the resulting atmospheric forcing are emerging as some of the main uncertainties associated with climate projections (Hansen et al. 1998; Prentice et al. 2001). In most previous anthropogenic climate change projections, the trajectory of atmospheric $CO_2$ concentration is prescribed and the resulting physical climate response computed. This approach, however, neglects the potential for substantial feedbacks between climate change and the carbon cycle that could either exacerbate or partially ameliorate global climate change.

Human perturbations to the earth's climate occur on top of a large natural carbon cycle—a complex system involving the ocean, atmosphere, and land domains and the fluxes among them. Many of the underlying ecological and biogeochemical processes are sensitive to shifts in temperature, the hydrological cycle, and ocean dynamics, and the magnitude and in some cases even the sign of specific carbon–climate feedbacks are unknown. Two recent studies by Cox et al. (2000) and Dufresne et al. (2002) present strikingly different pictures of carbon–climate feedbacks, differences that must arise because of the underlying formulations linking the physical climate and biogeochemistry (BGC). On geological time scales, ice core and other paleoproxy reconstructions suggest large contemporaneous variations in climate and atmospheric $CO_2$, ranging from glacial–interglacial cycles (Petit et al. 1999) to the high $CO_2$ warm periods of the Cretaceous and Permian; the exact interplay of climate forcing and carbon cycle dynamics on these scales is not well resolved either.

Numerical models provide one of the few direct and quantitative methods for assessing such questions, and a number of recent studies have explored the behavior of coupled carbon–climate simulations (Friedlingstein et al. 2001, 2006; Thompson et al. 2004; Zeng et al. 2004; Mathews et al. 2005; Govindasamy et al. 2005). Here we present a new fully coupled 3D climate–carbon cycle model based on the framework of the Community Climate System Model (CCSM) project (Blackmon et al. 2001). The overall objectives of the CCSM carbon project are to better understand the following: 1) what processes and feedbacks are most important in setting atmospheric $CO_2$, and 2) how do $CO_2$ and climate coevolve? We focus in this paper on the description of

the land, ocean, and atmosphere biogeochemical component models (section 2), their integration within the National Center for Atmospheric Research (NCAR) coupled atmosphere–land–ocean–ice physical climate model (CSM) 1.4 framework, and the analysis of a stable, 1000-yr preindustrial simulation. By introducing a sequential spinup procedure, we minimize the drifts in land and ocean carbon inventories that can arise from biases in the coupled model physical climate (section 3). In section 4, we assess the skill of the control simulation by comparing the annual mean and seasonal cycle of key simulated carbon metrics against observations. We fully resolve the 3D structure of atmospheric $CO_2$, providing important constraints on model dynamics. We then use the control integration to quantify the magnitude and physical mechanisms of natural interannual, decadal, and centennial variability in carbon exchange within and among the reservoirs (section 5). We conclude with a brief discussion and summary (section 6).

The simulations presented here focus on the carbon cycle responses to intrinsic natural variability of the physical climate system. We do not include natural external climate perturbations such as volcanic eruptions and solar variability that may impact carbon cycle variability (e.g., Gerber et al. 2003; Trudinger et al. 2005). Experiments using the CSM 1-carbon model, exploring the carbon–climate feedbacks arising from the anthropogenic fossil fuel $CO_2$ emissions for the nineteenth, twentieth, and twenty-first centuries, are presented in Fung et al. (2005). Key finds reported there include an inverse relationship between carbon sink strengths and the rate of fossil fuel emissions, a positive carbon–climate feedback where climate warming increases atmospheric $CO_2$ and amplifies the climate change, and large regional changes in terrestrial carbon storage, modulated by hydrologic and ecosystem responses.

## 2. Model description

The coupled carbon–climate model treats radiative $CO_2$ as a prognostic variable, with the atmospheric abundance as the residual after accounting for the climate-sensitive fluxes into and out of the land biosphere ($F_{ab}$ and $F_{ba}$, respectively), and into and out of the ocean ($F_{ao}$ and $F_{oa}$, respectively):

$$\frac{\partial}{\partial t} CO_2 + \Im(CO_2) = \text{ExternalSource} - F_{ab} + F_{ba} - F_{ao} + F_{oa}. \quad (1)$$

In Eq. (1), $\Im(CO_2)$ is the 3D atmospheric transport of $CO_2$, due to large-scale advection and to the turbulent mixing associated with dry and moist convection. We

have added Eq. (1) to CSM 1.4 and embedded new versions of a terrestrial carbon module to estimate $F_{ab}$ and $F_{ba}$ and an oceanic carbon module to estimate $F_{ao}$ and $F_{oa}$. These are described below. In the control run described here, ExternalSource = 0. The CSM 1.4-carbon source code and the simulations discussed here are available electronically (see online at http://www.ccsm.ucar.edu/working_groups/Biogeo/csm1_bgc/).

### a. CSM 1.4 coupled physical model

The core of the coupled carbon–climate model is a modified version of NCAR CSM 1.4, consisting of ocean, atmosphere, land, and sea ice physical components integrated via a flux coupler (Boville and Gent 1998; Boville et al. 2001). The simulations here are integrated with an atmospheric spectral truncation resolution of T31 (~3.75°) with 18 levels in the vertical, and an ocean resolution of 0.8°–1.8° latitude and 3.6° longitude with 25 levels in the vertical (referred to as T31 × 3). The sea ice component model runs at the same resolution as the ocean model, and the land surface model runs at the same resolution as the atmospheric model. Physical control simulations display stable surface temperatures and minimal deep ocean drift without requiring surface heat or freshwater flux adjustments. The water cycle is closed through a river runoff scheme, and modifications have been made to the ocean horizontal and vertical diffusivities and viscosities from the original version (CSM 1.0) to improve the equatorial ocean circulation and interannual variability.

The 3D atmospheric $CO_2$ distribution is advected and mixed as a dry-air mixing ratio using a semi-Lagrangian advection scheme; both dry and moist turbulent mixing schemes are used for the transport of water vapor mass fractions. The model $CO_2$ field affects the shortwave and longwave radiative fluxes through the column average $CO_2$ concentration.

### b. Land carbon cycle model

The CSM 1.4-carbon land carbon module (Fig. 1) combines the NCAR Land Surface Model (LSM) biogeophysics package (Bonan 1996) with the Carnegie–Ames–Stanford Approach (CASA) biogeochemical model (see Randerson et al. 1997). Both the LSM and CASA models are documented extensively in the literature. Here we provide a brief overview of the models and highlight changes that have been made to the standard model dynamics. The land surface is characterized by the fractional coverage of 14 plant functional types (PFTs) and 3 soil textures (Bonan 1996). LSM estimates leaf-level stomatal conductance of $CO_2$ and
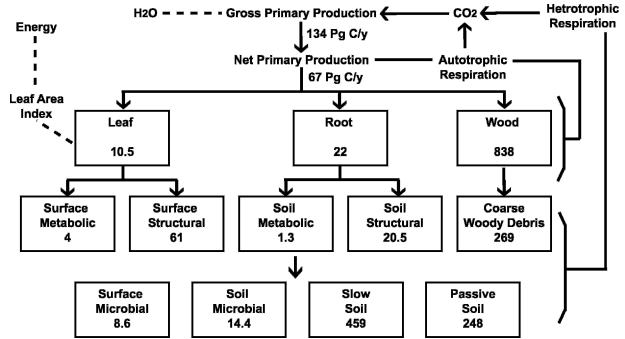


FIG. 1. Schematic of land biogeochemistry module in CSM 1.4-carbon based on modified versions of the NCAR LSM and CASA biogeochemical parameterizations (Bonan 1996; Randerson et al. 1997). Simulated NPP (Pg C $yr^{-1}$) on land is computed as the difference between GPP, provided by LSM, thus linking carbon uptake with stomatal water loss and autotrophic respiration. NPP is allocated to three biomass pools (leaf, wood, and root), and heterotrophic respiration and detrital material are incorporated through nine detrital and soil carbon pools. Prognostic leaf phenology and dynamic allocation are also incorporated. The land biogeochemical modules affect the physical climate water and energy cycles through varying LAI and GPP. The mean carbon standing stocks (Pg C) for each of the living and detrital pools are shown for the 1000-yr control integration.

water to maximize carbon assimilation for sunlit and shady conditions (Collatz et al. 1990; Sellers et al. 1996). The carbon assimilation is integrated through the canopy using the fraction of sunlit and shade leaves to yield gross primary productivity (GPP). A terrestrial $CO_2$ fertilization effect arises physiologically in the model because carbon assimilation via the Rubisco enzyme is limited by internal leaf $CO_2$ concentrations; GPP thus increases with external atmospheric $CO_2$ concentrations, eventually saturating at high $CO_2$ levels.

In this implementation, net primary productivity (NPP = $F_{ab}$) is assumed to be 50% of GPP calculated by LSM (replacing NPP calculated by CASA). The NPP/GPP ratio has been demonstrated to be constant on annual time scales across a wide range of forests (Waring et al. 1998). While it is well known that autotrophic respiration ($R_a$) varies seasonally and diurnally, we have not modeled $R_a$ explicitly, as its magnitude as well as sensitivity to temperature and other control variables remain uncertain even in high-frequency flux tower measurements (e.g., Wohlfahrt et al. 2005; Reichstein et al. 2005). The impact of this assumption on modeled $CO_2$ cannot be readily quantified, as global-scale constraints are available for the seasonal variability of NPP [via satellite observations of the normalized difference vegetation index (NDVI)] and on the net flux (via the seasonal oscillations of atmospheric $CO_2$), and not for GPP or respiration.

NPP is allocated to three live biomass pools $M$ (leaf,

wood, and root) following Friedlingstein et al. (1999), with preferred allocation to roots during water-limited conditions and to leaves during light-limited conditions:

$$\frac{\partial}{\partial t} M_k = \alpha_k \mathrm{NPP} - \frac{M_k}{\tau_k} \quad k = 1, 2, 3. \quad (2)$$

In the CASA formulation, turnover times $\tau_k$ of the three live pools are PFT specific but time invariant, with constants ranging from 1.8 yr for leaves in tropical broadleaved evergreen trees to 48 yr for wood in broad-leaved deciduous tress. The leaf mortality of deciduous trees is modified to include cold-drought stress to effect leaf fall in 1–2 months, and leaf biomass (kg C m$^{-2}$ land) is translated into prognostic leaf area indices (LAI) using specific leaf areas [SLA; m$^{-2}$ leaf (kg C)$^{-1}$] following Dickinson et al. (1998), so that LAI vary with climate. We place limits on LAI, with a minimum of 0.6 to simulate the storage of carbon in photosynthates and a maximum of 6 to simulate light and nutrient limitation. The excess carbon above the maximum $M_{\mathrm{leaf}}$ is added to litterfall $M_{\mathrm{leaf}}/\tau_{\mathrm{leaf}}$.

There are nine dead carbon pools, with leaf mortality contributing to metabolic and structure surface litter ($k = 4, 5$), root mortality contributing to metabolic and structure soil litter ($k = 6, 7$), and wood mortality contributing to coarse woody debris (CWD; $k = 8$). The subsequent decomposition of $M_k$, $k = 4$–8 by microbes leads to the transfer of carbon to the dead surface, soil microbial pools ($k = 9, 10$), and the slow and passive pools ($k = 11, 12$). A fraction of each carbon transfer is released to the atmosphere via microbial or heterotrophic respiration. This is summarized in Eq. (3):

$$\frac{\partial}{\partial t} M_k = \sum_{j=1}^{12} \gamma_{jk} \frac{M_j}{\tau_j} - \sum_{n=4}^{12} \gamma_{kn} \frac{M_k}{\tau_k}$$

$$- \left(1 - \sum_{n=4}^{12} \gamma_{kn}\right) \frac{M_k}{\tau_k} \quad k = 4, \ldots 12. \quad (3)$$

The first term on the rhs of Eq. (3) is the gain of $M_k$ due to litterfall and the transfer from other dead carbon pools $j$; the second term is the loss of $M_k$ due to transfer from pool $k$ to other pools $n$; and the third term is $R_h = F_{\mathrm{ba}}$, the loss of carbon to the atmosphere via heterotrophic respiration. The transfer coefficients $\gamma_{jk}$ are time-invariant constants following CASA.

The rates of transfer are climate sensitive, following CASA:

$$\tau_k^{-1} = \tau_{k0}^{-1} f(T) g(w) \quad k = 4, \ldots 12, \quad (4)$$

where $\tau_{k0}$ is the turnover time of pool $k$ at 10°C with no water limitation; $\tau_{k0}$ ranges from 20 days for the metabolic soil pool to 500 yr for the passive pool. The modu-

lators $f(T)$ and $g(w)$ are functions of soil temperature ($T$) and an index of soil moisture saturation ($w$), respectively. Soil temperature and soil moisture are averaged over the top 30 cm (top two model soil layers) of the soil. Here, $f(T)$ is represented by a $Q_{10}$ of 2, or a rate doubling for every 10°C increase in soil temperature referenced to 10°C, and $g(w)$ is a monotonic function of soil moisture saturation, and ranges linearly between 0 and 1 for $w$ between 0.25 and 0.75.

This version of the model does not include other land surface processes that affect atmosphere–biosphere interactions. These include an explicit nitrogen cycle, fires and other disturbances, herbivory, dynamic vegetation cover, or anthropogenic land cover change.

Carbon fluxes and carbon pools are updated at LSM time steps of 30 min so that the prognostic biogeochemistry is in step with the biogeophysics. The geographic distribution of the net atmosphere–land flux,

$$\Delta F_{\mathrm{land}} = F_{\mathrm{ab}} - F_{\mathrm{ba}} = \mathrm{NEP} = \mathrm{NPP} - R_h, \quad (5)$$

is passed to the atmosphere to update atmospheric $CO_2$ concentration. In this way, changes in leaf areas calculated by CASA influence GPP transpiration and albedo, while changes in temperature and soil moisture calculated by LSM alter NPP, allocation and decomposition rates. Thus, there is full coupling of the energy, water, and carbon cycles.

## c. Ocean carbon cycle model

The ocean carbon cycle model is a derivative of the Ocean Carbon Model Intercomparison Project (OCMIP-2) biotic carbon model, which is itself a derivative of the model of Najjar et al. (1992), and is described, for instance, in Doney et al. [2003, 2004; see also R. G. Najjar and J. C. Orr 1999, unpublished manuscript (OCMIP-2 Biotic-HOWTO; available online at http://www.ipsl.jussieu.fr/OCMIP/)]. Air–sea fluxes of $CO_2$ are estimated as

$$\Delta F_{\mathrm{ocn}} = F_{\mathrm{ao}} - F_{\mathrm{oa}} = k_u \beta_T (p\mathrm{CO}_2^{\mathrm{atm}} - p\mathrm{CO}_2^{\mathrm{sw}})(1 - f_{\mathrm{ice}}),$$

$$(6)$$

where $k_u$ is the wind-dependent gas exchange coefficient across the air–sea interface, $\beta_T$ is the temperature-dependent solubility of $CO_2$, $p\mathrm{CO}_2^{\mathrm{atm}}$ and $p\mathrm{CO}_2^{\mathrm{sw}}$ are the partial pressures of $CO_2$ in the lowest two layers of the atmosphere ($\sim$60 mb) and in the top layer of the ocean, respectively, and $f_{\mathrm{ice}}$ is the fractional ice coverage. The $p\mathrm{CO}_2^{\mathrm{sw}}$ is calculated from model dissolved inorganic carbon (DIC), alkalinity (ALK), temperature, and salinity according to carbonate chemistry.

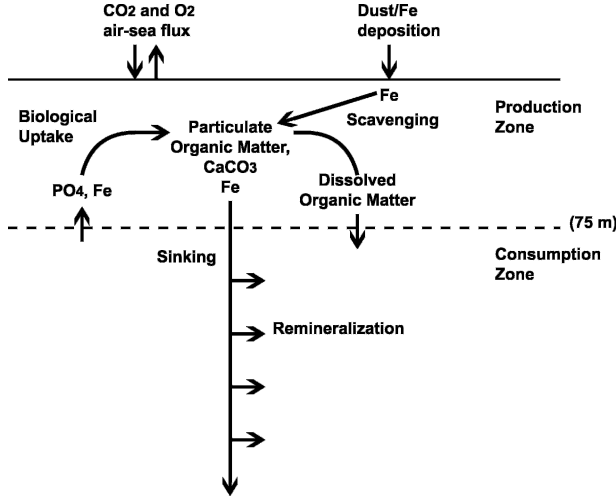The primary differences between the new model (Fig. 2) and the OCMIP-2 BGC model are

FIG. 2. Schematic of ocean biogeochemistry module in CSM 1.4-carbon based on a modification of the OCMIP-2 biotic carbon parameterization (Doney et al. 2003). The model includes (in simplified form) the main processes for the solubility carbon pump, organic and inorganic biological carbon pumps, and air–sea $CO_2$ flux. Modifications from the original OCMIP-2 version include the prognostic computation of new/export production as a function of light, temperature, phosphate and iron concentrations, and a dynamical iron cycle.

- nutrient uptake has been changed from a nutrient restoring formulation to a prognostic formulation,
- iron has been added as a limiting nutrient in addition to phosphate, and
- a parameterization for the iron cycle has been introduced.

The prognostic variables transported in the ocean model are phosphate ($PO_4$), total dissolved inorganic Fe, dissolved organic phosphorus (DOP), DIC, ALK, and oxygen $O_2$. Here we only describe the differences with the OCMIP-2 biotic carbon model.

1) NUTRIENT UPTAKE

The parameterization of biological uptake is similar to that used in the Hamburg Model of the Ocean Carbon Cycle (HAMOCC; Bacastow and Maier-Reimer 1990; Maier-Reimer 1993). The uptake of $PO_4$ is given by the turnover of biomass $B$, modulated by temperature, macro- and micronutrients, and surface solar irradiance:

$$J_{\text{prod}} = F_T \cdot F_N \cdot F_I \cdot B \cdot \max(1, z_{ml}/z_c)/\tau. \qquad (7)$$

Like the OCMIP-2 BGC model, biological uptake only occurs in the production zone ($z < z_c$), where $z_c$ is the compensation depth (75 m). The temperature limitation function,

$$F_T = (T + 2)/(T + 10), \qquad (8)$$

is the same that is used in HAMOCC with $T$ (°C). The nutrient limitation term is the minimum of Michaelis–Menten limiting terms for $PO_4$ and Fe:

$$F_N = \min\left(\frac{PO_4}{PO_4 + \kappa_{PO4}}, \frac{Fe}{Fe + \kappa_{Fe}}\right), \qquad (9)$$

where $\kappa_{PO4}$ is 0.05 $\mu$mol L$^{-1}$ and $\kappa_{Fe}$ is 0.03 nmol L$^{-1}$. The light (irradiance) limitation term,

$$F_I = \frac{I}{I + \kappa_I}, \qquad (10)$$

uses $I$, the solar shortwave irradiance, and a light limitation term $\kappa_I$ (20 W m$^{-2}$). Irradiance decays exponentially from the sea surface with a 20-m length scale. If the cell is completely contained in the mixed layer $z_{ml}$, then $I$ is the average over the entire mixed layer. If the cell is completely below in the mixed layer, then $I$ is simply the average over the cell. For intermediate cases, $I$ is the appropriate weighted average. As a consequence, the light limitation term decays like $O(1/z_{ml})$ for $z_{ml} > z_c$. $B$ is a proxy for biomass ($\mu$mol L$^{-1}$):

$$B = \min\left(PO_4, \frac{Fe}{r_{Fe:P}}\right), \qquad (11)$$

where $r_{Fe:P}$ is the ratio of Fe to $PO_4$ uptake $5.85 \times 10^{-4}$ (mol/mol), derived by assuming a Fe-to-C uptake ratio of $5.0 \times 10^{-6}$ (mol/mol) and a C-to-$PO_4$ uptake ratio of 117 (mol mol$^{-1}$). The term $\max(1, z_{ml}/z_c)$ scales the uptake by $z_{ml}$ when it exceeds $z_c$; this is meant to implicitly extend the production zone to the base of the mixed layer. Finally, $\tau$ is the optimal uptake time scale (15 days).

2) IRON PARAMETERIZATION

There are three conceptual forms of iron in the model: Fe representing dissolved inorganic iron, DOFe representing the iron content of the dissolved organic matter, and POFe representing the iron content of the sinking particles. The following processes govern the iron cycle:

- surface deposition of Fe from the atmosphere,
- biological uptake of Fe, converting Fe into DOFe and POFe,
- remineralization of DOFe into Fe,
- scavenging of Fe into POFe,
- and remineralization of POFe into Fe.

Surface deposition of Fe is derived from the monthly climatological dust flux estimated by Mahowald et al. (2003). The dust is assumed to be 3.5% Fe by weight with 2% of the Fe bioavailable. Biological uptake of Fe

is equal to $r_{Fe:P} \times J_{prod}$. It is routed to DOFe and POFe using the same partitioning that is used for P, where a fixed fraction $\sigma = 0.67$ goes to DOFe and the remainder goes to POFe. DOFe remineralizes into Fe following first-order kinetics with a rate constant $\kappa = 2 \text{ yr}^{-1}$. Since $r_{Fe:P}$ is constant and $\sigma$ and $\kappa$ are the same for the Fe pools as they are for the P pools, DOFe is equal to $r_{Fe:P} \cdot$ DOP. Because of this relationship, DOFe is not explicitly tracked in the model.

The scavenging of Fe is similar to the single ligand model described in Archer and Johnson (2000). Conceptually, there is a ligand that organically binds to Fe molecules, protecting them from scavenging; Fe that is not bound to ligands is denoted $Fe_{free}$ and is the positive root of the quadratic equation

$$Fe_{free}^2 + (L + 1/K_L - Fe)\,Fe_{free} - Fe/K_L = 0, \quad (12)$$

where $L$ is the concentration of ligand and $K_L$ is the strength of the binding reaction. We assume a globally uniform ligand concentration of 1.0 nmol $L^{-1}$ and a $K_L = 300$ L(nmol)$^{-1}$. The scavenging of Fe is given by

$$J_{Fe\_scav} = Fe_{free}\, C_0[1 + \alpha \exp(-z/z_{scav})], \quad (13)$$

where $C_0 = 0.2 \text{ yr}^{-1}$, $\alpha = 200$, and $z_{scav} = 250$ m.

Scavenged Fe is attached to the sinking particles to form POFe. A fraction (40%) of the scavenged Fe is assumed to be insoluble and is directly lost to the sediments. The remaining 60% can be remineralized back to dissolved form below $z_c$. The OCMIP-2 model used a single Martin power-law curve (a = −0.9) to describe the vertical POP flux profile over all the full water column. This scheme needs to be modified to a local power law because scavenged Fe is attached to the sinking organic matter throughout the water column. Consider a model cell with a flux $F_{POFe}$ through the top at $z_t$. The flux at the bottom ($z_b$) is then

$$F_{POFe}(z_b) = F_{POFe}(z_t) \cdot (z_b/z_t)^{-a}$$
$$+ (z_b - z_t) \cdot 0.6 \cdot J_{Fe\_scav}, \quad (14)$$

where 0.6 represents the 60% of the scavenged Fe that is potentially soluble. Of the POFe that reaches the seafloor, that due to biological uptake is remineralized into the bottom cell. This is equivalent to setting the seafloor remineralization of POFe to $r_{Fe:P}$ times seafloor POP remineralization.

## 3. Coupled carbon–climate spinup

To reduce the magnitude of the coupling shock and transient response when carbon is coupled to the climate of the coupled model, a sequential spinup procedure is employed (Fig. 3). The spinup procedure involves categorizing atmospheric $CO_2$ into three flavors:

**CSM 1.4-Carbon (T31/x3) Spin-up**

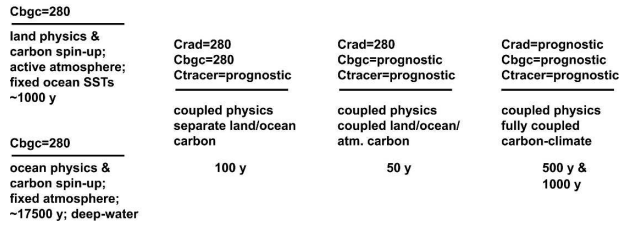| Cbgc=280 land physics & carbon spin-up; active atmosphere; fixed ocean SSTs ~1000 y | Crad=280 Cbgc=280 Ctracer=prognostic | Crad=280 Cbgc=prognostic Ctracer=prognostic | Crad=prognostic Cbgc=prognostic Ctracer=prognostic |
|---|---|---|---|
| | coupled physics separate land/ocean carbon | coupled physics coupled land/ocean/ atm. carbon | coupled physics fully coupled carbon-climate |
| Cbgc=280 ocean physics & carbon spin-up; fixed atmosphere; ~17500 y; deep-water | 100 y | 50 y | 500 y & 1000 y |

FIG. 3. Schematic of the sequential spinup procedure used to reduce physical and biogeochemical drift for CSM 1.4-carbon control simulation. The spinup procedure involves categorizing atmospheric $CO_2$ into three flavors: $C_{BGC}$ is the concentration seen by the land biosphere and ocean, $C_{Tracer}$ is the concentration advected in the atmosphere, and $C_{Rad}$ is the concentration seen by the physical climate radiation code. Two multicentury control simulations are conducted. In our standard 1000-yr control, $C_{BGC}$ seen by the land is fixed at 280 ppmv; this is equivalent to assuming that there is no terrestrial $CO_2$ fertilization production and that production is limited by other factors such as nitrogen. A companion 500-yr experiment includes the full effects of $CO_2$ fertilization on terrestrial photosynthesis. The mean state and variability of the two simulations are indistinguishable statistically in both physical and biogeochemical measures.

- Tracer $CO_2$ ($C_{Tracer}$): This flavor is transported by the atmospheric dynamics and responds to the geographically varying surface fluxes provided by the land and ocean components.
- Biogeochemistry $CO_2$ ($C_{BGC}$): This flavor is passed to the land and ocean components for inclusion in photosynthesis and air–sea flux computations. It is either a specified constant (e.g., 280 ppm for preindustrial conditions) or taken to be the model time–space varying $C_{Tracer}$ field averaged in the vertical over the bottom two model levels (~60 mb). The specification could be different for the land and the ocean.
- Radiative $CO_2$ ($C_{Rad}$): This flavor is passed to the atmospheric component's radiation parameterization. It is either a specified constant or is taken to be the (pressure weighted) column average of $C_{Tracer}$. Note that in traditional climate models, $C_{Rad}$ depends only on time; in this study, we additionally allow $C_{Rad}$ to vary with latitude and longitude. The CSM 1 atmospheric radiation parameterization makes numerous simplifications based on the assumption that $C_{Rad}$ is vertically homogeneous, making it impractical to include the vertical distribution of $C_{Tracer}$. However, independent computations indicate that the impact of including the vertical distribution of $CO_2$ in the radiation calculations is negligible (J. Kiehl 2003, personal communication).

The land and ocean carbon components are first spun up to an approximate steady state and then incremen-

tally coupled with each other and the physical climate. For the ocean circulation and carbon model spinup, we use prescribed atmosphere physics and sea ice observational datasets that correspond to modern conditions. Atmospheric $CO_2$ ($C_{BGC}$) is held at 278 ppm, representing preindustrial conditions. Integrating the ocean model to a steady state would take thousands of model years. To avoid such a long integration, a depth-dependent acceleration technique is used following Danabasoglu et al. (1996). Because this technique is not conservative, $PO_4$, DOP, and ALK are multiplied by a scale factor at the beginning of each year to restore the global inventories of $PO_4$ + DOP and ALK − $r_{N:P}$ DOP. The ocean model is run for 350 surface years, corresponding to 17 500 accelerated deep-water years, at which point the annual air–sea $CO_2$ gas flux is 0.063 ± 0.011 Pg C $yr^{-1}$ over the last 10 yr of the integration.

The land carbon component is particularly sensitive to soil moisture, so it is expeditious for the hydrological cycle in the land spinup to resemble that of a coupled simulation. The approach taken here is to start with $M_k$ produced by a 1000-yr integration of the land carbon module forced by the CSM 1.4 surface climate and to generate coupled carbon–climate model climatologies from a preliminary 100-yr run with all active physical components and land carbon ($C_{BGC}$ = $C_{Rad}$ = 280 ppm). This step yields approximate steady states for NPP and the live carbon pools under the coupled model climate. The detrital and soil carbon pools are next spun up in an offline mode forced by the coupled carbon–climate model climatologies of litterfall, surface air, soil temperatures, and soil moisture. The land spinup is then continued with active atmospheric and land components ($C_{BGC}$ = $C_{Rad}$ = 280 ppm) and data cycling of the model climatologies of SST and ice extent. Additional numerical acceleration techniques are applied during this phase to the slow and passive soil carbon pools, which have turnover times in excess of 200 yr and thus would require over 1000 yr to fully equilibrate. The final net land $CO_2$ flux over the last 10 yr of the land spinup is 0.072 ± 0.613 Pg C $yr^{-1}$.

The end states of the land and ocean carbon spinups are inserted into a full physically coupled atmosphere–ocean–land–ice configuration and are then incrementally coupled to the physics and each other. In a first 100-yr segment (Fig. 3), $C_{BGC}$ and $C_{Rad}$ are fixed at 280 ppm in order to allow the land and ocean carbon cycles to adjust to the climate of the coupled model. The land and ocean carbon components at this step are thus independent. In a second 50-yr segment, $C_{Tracer}$ is reinitialized to 280 ppmv, $C_{BGC}$ (for the land and ocean) is the average of the lowest ~60 mb of $C_{Tracer}$, and $C_{Rad}$ remains set to 280 ppm. The purpose of this segment is

to allow the land and ocean carbon cycles to adjust to each other via $C_{Tracer}$ prior to the introduction of radiative feedbacks. The end state of the second segment has a global mean atmospheric $CO_2$ concentration of ~282 ppmv and net $CO_2$ fluxes of 0.17 ± 0.74 Pg C $yr^{-1}$, and it is used as the initial condition of the 1000-yr control run, where $C_{Rad}$ varies with $C_{Tracer}$, providing full prognostic carbon–climate coupling. Note that $C_{Tracer}$ is not reset at the beginning of the control run. Because of this and the fact that the system conserves carbon, the total carbon inventory for the 1000-yr control model is determined by the initial conditions of the second segment, and is in equilibrium with an atmospheric $CO_2$ of ~280 ppmv and the corresponding model climate.

In our standard 1000-yr control, we do not use the prognostic $C_{BGC}$ for the land biosphere; $C_{BGC}$ seen by the land is fixed at 280 ppmv. This is equivalent to assuming that there is no terrestrial $CO_2$ fertilization production and that production is limited by other factors such a nitrogen. A companion 500-yr experiment includes the full effects of $CO_2$ fertilization on terrestrial photosynthesis by setting $C_{BGC}$ to be the evolving $CO_2$ concentration in the lowest ~60 mb of the atmosphere. The mean state and variability of the two simulations are statistically indistinguishable in both physical and biogeochemical measures, reflecting the fact that the natural variations in atmospheric $CO_2$ in our control simulations are relatively small.

## 4. Model stability and mean physical/biogeochemical climate

### a. Global climate and carbon cycle time series

As shown in Fig. 4, global integral properties such as the average surface temperature, atmospheric $CO_2$ concentration, and the ocean and land carbon inventories remain approximately stable over the entire 1000-yr coupled carbon–climate control simulation. Global annual mean model surface temperature remains constant within ±0.10 K (1 $\sigma$) over the integration, and other global integral physical climate metrics are similarly constant. The stability of the CSM 1 physical climate with fixed atmospheric composition and no flux corrections is documented in Boville and Gent (1998) and Boville et al. (2001). The global annual mean atmospheric $CO_2$ in the 1000-yr control run displays no long-term trend, and the variations are ±1.2 ppmv (1 $\sigma$), small enough that the concomitant alterations in the radiation budget are relatively minor. Thus, the variability in Fig. 4 arises from natural, internal dynamics of the climate system working on the carbon cycle.

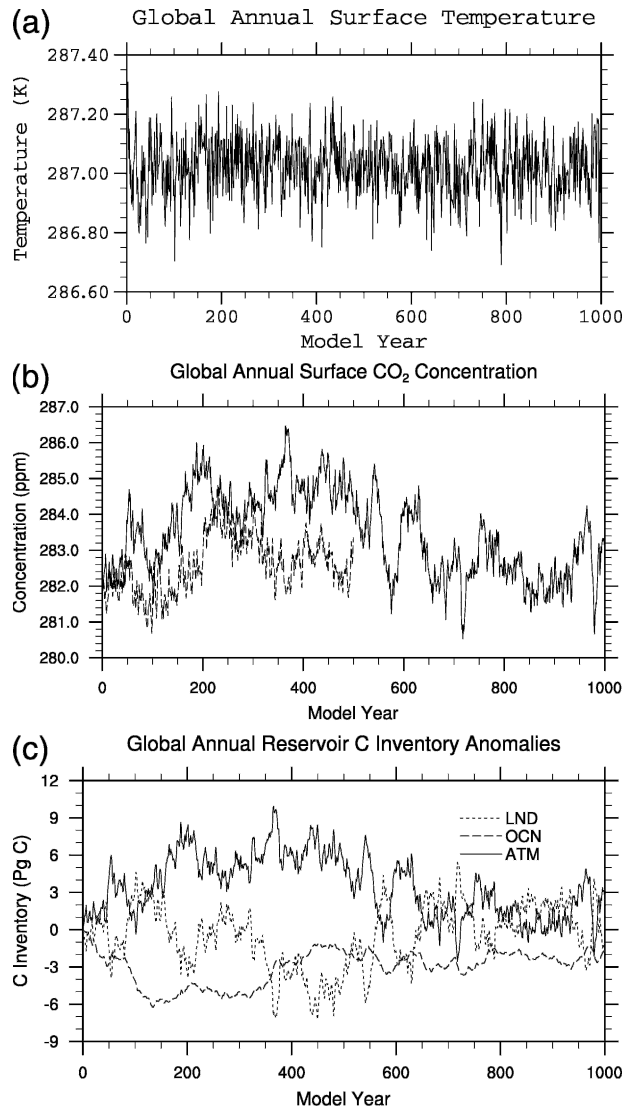The model carbon inventories vary on interannual-

**(a)** Global Annual Surface Temperature

**(b)** Global Annual Surface CO$_2$ Concentration

**(c)** Global Annual Reservoir C Inventory Anomalies

FIG. 4. Time series of annual mean global (a) surface temperature (K), (b) surface atmospheric CO$_2$ concentration (ppmv dry air), and (c) atmosphere, land, and ocean carbon inventory anomalies (Pg C) from the CSM 1.4-carbon 1000-yr control simulation. The dashed line in (b) is the surface atmospheric CO$_2$ concentration from a companion 500-yr control simulation with land biosphere CO$_2$ fertilization.

to-centennial time scales, reflecting continuous repartitioning of carbon among the atmosphere, ocean, and land reservoirs (Fig. 4c). A dominant feature is the gradual increase in atmospheric CO$_2$ by ~4 ppmv in the first 350–400 yr of the integration followed by a comparable decrease over the ensuing 200–250 yr. These changes are tied to oscillations in both the land and ocean inventories and are related to slow adjustments in the physical climate (soil moisture, land and sea surface temperatures, ocean circulation) and, for the oceans, changes in atmospheric CO$_2$. The 500-yr simu-

lation with CO$_2$ fertilization also exhibits a stable but somewhat different atmospheric CO$_2$ trajectory (Fig. 4b); in this case there is an initial transient uptake rather than release from the land biosphere. The magnitude of the interannual-to-centennial variability is quite comparable, however.

Superposed on the very low-frequency variations are centennial and shorter time-scale signals, which dominate the variability in the last 400 yr of the 1000-yr control simulation. Because it is difficult to separate the effects of model drift from natural variability on the millennial time scale with only a 1000-yr simulation, we focus our analysis on centennial and shorter time scales. These variations in atmospheric inventory appear to be driven primarily by changes in the land inventory, with net terrestrial carbon uptake and release events as large as 5–10 Pg C on decadal scales. On these same scales, the ocean carbon inventory is positively correlated with the atmosphere and anticorrelated with the land, but with a smaller amplitude signal (~10%–20%). The dynamics controlling this variability are discussed in more detail in section 5.

### b. Physical climate drift and biases

Similar to previous physics-only CSM 1 solutions, the carbon–climate control simulation is not completely stationary, exhibiting long-term drift in some physical properties. There is a vertical redistribution of salt in the ocean with the surface ocean freshening (~0.035 psu century$^{-1}$) and a corresponding increase of deep-water salinity. A small net heat flux imbalance leads to a weak ocean warming (~0.02 K century$^{-1}$ averaged over a full water column). The surface warming and freshening would both contribute to a small ocean CO$_2$ outgassing, but the flux is small relative to the internal variability of the model or the anthropogenic fluxes explored in Fung et al. (2005). The global storage of soil moisture and the biogeochemical moisture dependence term show little or no long-term drift. Nonnegligible patterns of regional climate drift occur but do not significantly impact our main findings.

There are also a number of biases in the spatial patterns of the physics in the CSM 1.4 coupled model that impact the biogeochemical solution. Model surface temperatures are too cold in the Northern Hemisphere continental interiors relative to observations (Fig. 5a). Although some of the cooling may be ascribed to the fact that our control run has preindustrial atmospheric CO$_2$ concentrations, other simulations with greenhouse forcing equivalent to the late twentieth century also show similar biases from −2 to −6 K (Boville et al. 2001; Dai et al. 2001). The CSM 1.4 solutions produce an

(a) Surface Temperature, Model - NCEP
mean = -0.65          rmse = 2.78          K

Min = -17.03 Max = 12.35

(b) Precipitation Rate, Model - GPCP
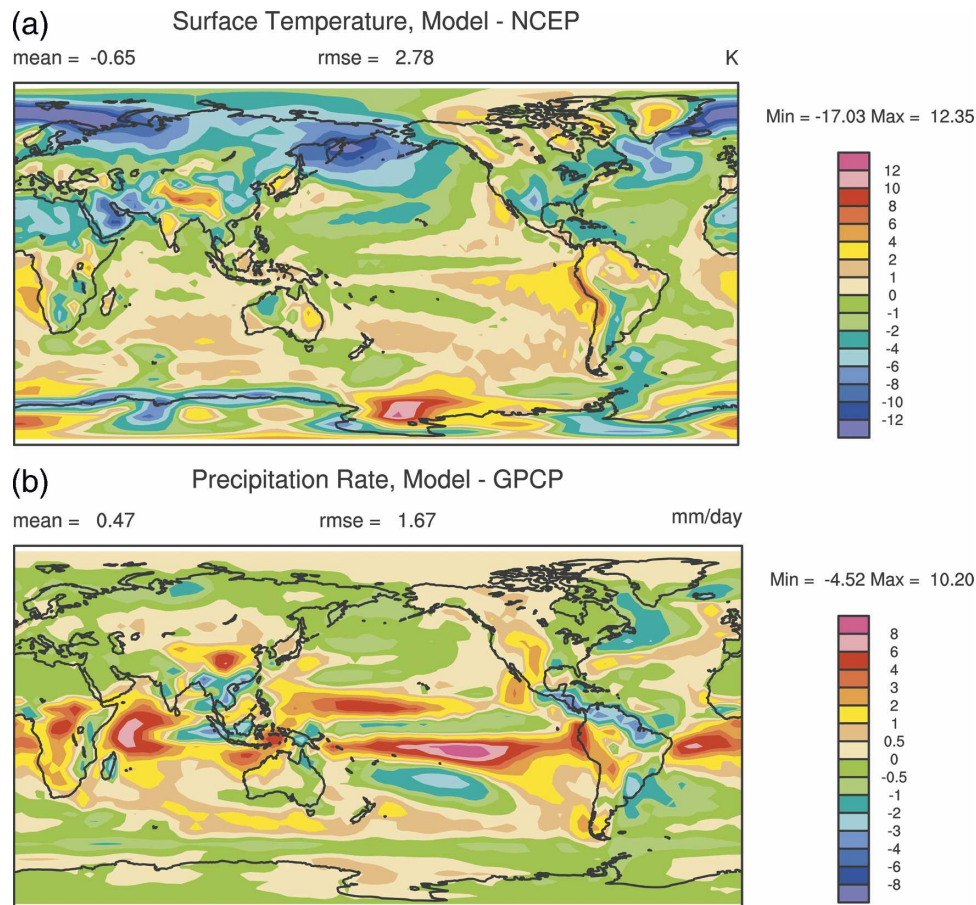mean = 0.47          rmse = 1.67          mm/day

Min = -4.52 Max = 10.20

FIG. 5. Spatial maps of annual mean physical biases of the CSM 1.4-carbon control simulation relative to modern climatological observations for (a) temperature (K; model minus NCEP) and (b) precipitation [mm day$^{-1}$; model minus Global Precipitation Climatology Project (GPCP)].

unrealistic precipitation pattern in the equatorial Pacific pattern with a double intertropical convergence zone (ITCZ) and bands of excess rainfall north and south of the equator (Boville and Gent 1998; Dai et al. 2001). Significant biases exist in tropical and temperate land precipitation with too wet conditions in central Africa, western South America, western North America, and parts of Indonesia, and with overly dry conditions in parts of Amazonia and eastern North America. In the model ocean, the double ITCZ leads to bands of too fresh and vertically stratified surface waters in the Pacific and to an off-equator shift in the maxima of interannual air–sea $CO_2$ flux variability (section 5b). On land, the temperature and precipitation biases result in corresponding anomalies in the simulated spatial patterns of NPP, LAI, and carbon storage.

*c. Land carbon dynamics*

The net terrestrial $CO_2$ flux $\Delta F_{land}$, or net ecosystem production (NEP), reflects the lag on seasonal interannual out to centennial time scales between NPP and heterotrophic respiration $R_h$. The global mean terrestrial NPP is 66.74 ± 0.88 Pg C yr$^{-1}$ in the 1000-yr control run. We note that the simulation is not directly comparable with contemporary observations because of land cover changes and climates forcings in the past two centuries, but the modeled NPP is within the range simulated by dynamic vegetation models forced by the climate of the nineteenth and twentieth centuries (Cramer et al. 2001). The geographic distribution of the simulated NPP (Fig. 6a) is not inconsistent with in situ measurements and satellite observations of the NDVI (e.g., Tucker et al. 2005). The latitudinal gradient of NPP is steeper than observed, with an underestimation at high latitudes due to the small area of boreal forests in the LSM prescriptions of plant functional types, the high-latitude cold bias in CSM 1.4, and an overestimation at low latitudes of excessive stomatal conductance under diffuse radiation. Some obvious blemishes in the simulated NPP field, such as the relatively low simu-
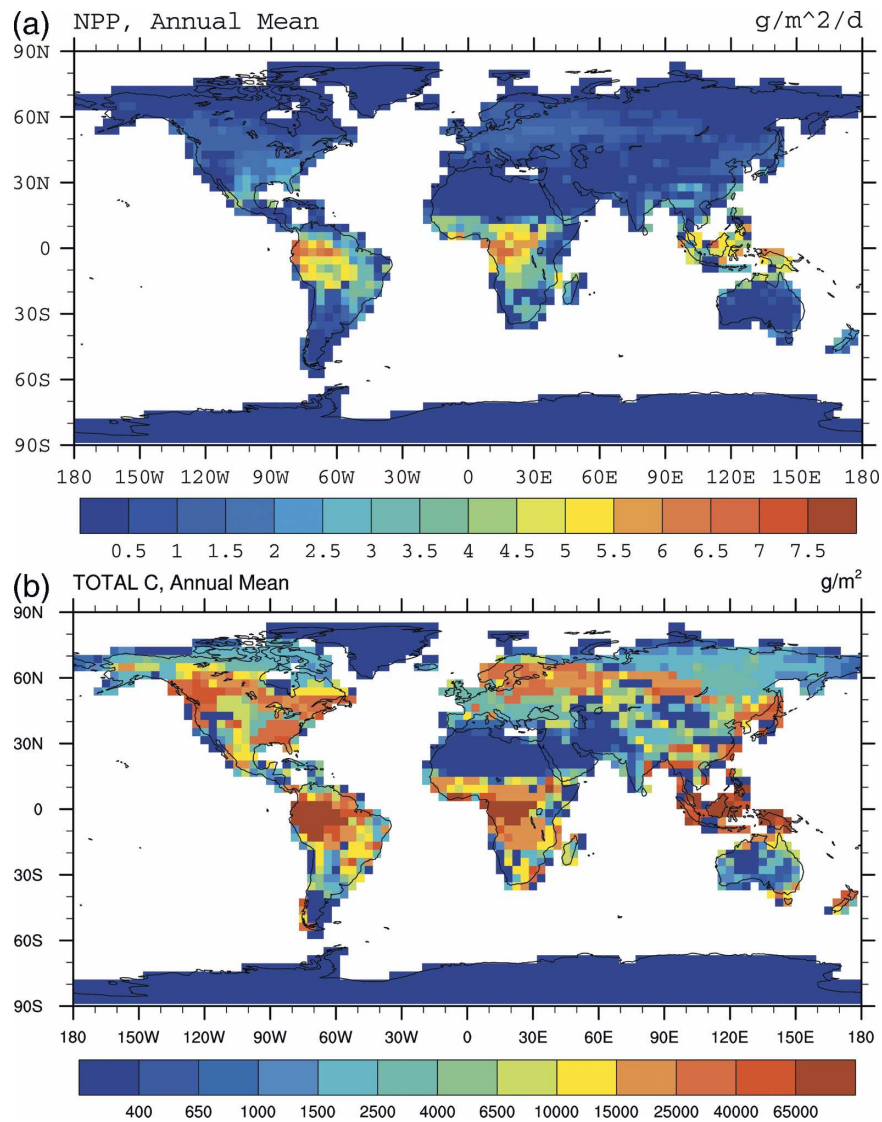
FIG. 6. Spatial maps of terrestrial (a) annual NPP (g C m$^{-2}$ yr$^{-1}$) and (b) total carbon storage (g C m$^{-2}$) averaged over the 1000-yr CSM 1.4-carbon control simulation.

lated values along the coast of eastern South America or in Indochina, are a direct result of biases in the coupled model precipitation field (Fig. 5b).

With the turnover times $\tau$ specified via the land carbon module [Eqs. (2)–(4)], the simulated NPP field yields reasonable distributions of living biomass and detrital/soil carbon—871 ± 2.4 and 1086 ± 2.0 Pg C, respectively (Figs. 1 and 6b). Substantial terrestrial carbon storage occurs in the regions of high NPP in the Tropics and subtropics, mostly in living biomass. Elevated carbon inventories are found as well along a band of boreal forests in the Northern Hemisphere associated with cooler temperatures and a larger fraction of storage in the detrital and soil pools. While the

model inventories are reasonable to the lowest order, it is difficult to directly compare the model detrital and soil carbon distribution against the observations. The model soil carbon pools represent only the organic material in the upper 20 cm of the soil, and the model does not account for carbon storage in high-latitude peats, for example.

### d. Ocean carbon dynamics

The geographic pattern of the average annual net air–sea flux (Fig. 7a) from the control simulation broadly resembles that compiled by Takahashi et al. (2002) for the contemporary ocean, showing net outflux of $CO_2$ from the equatorial regions and Southern
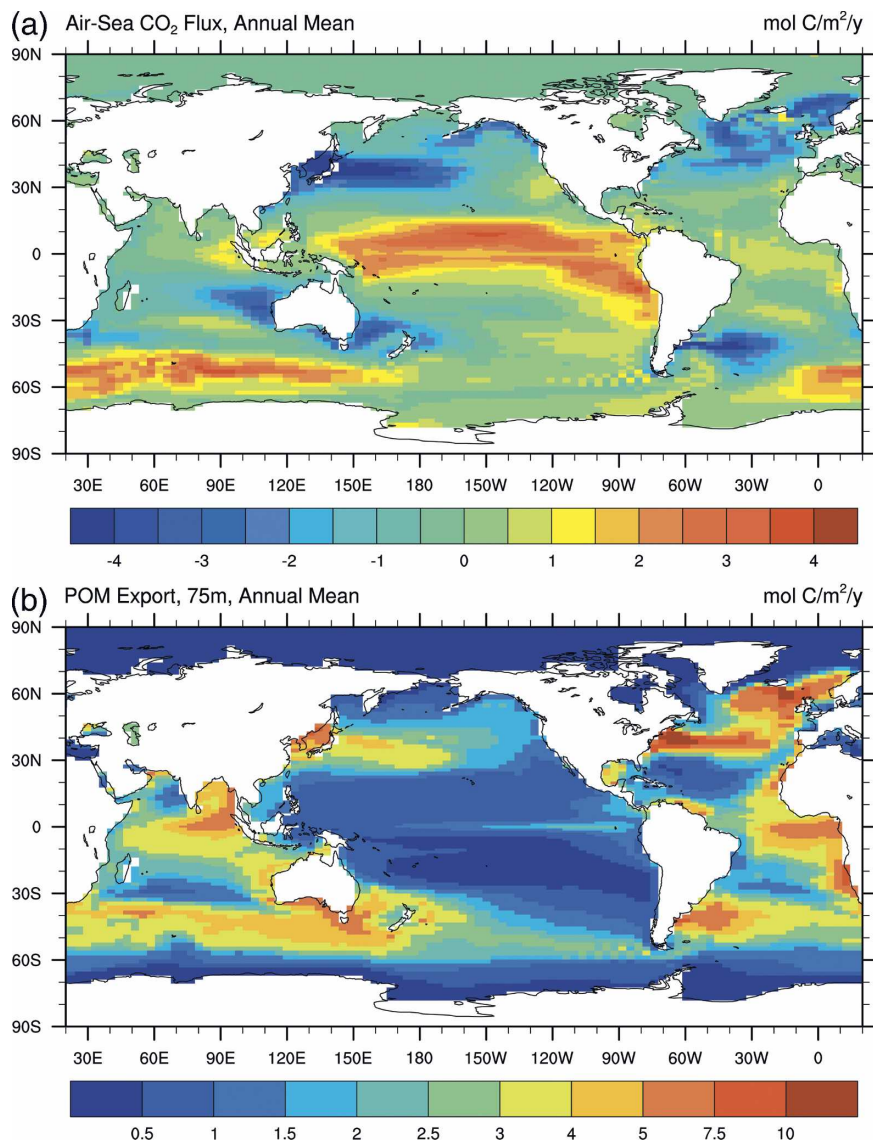
FIG. 7. Spatial maps of (a) annual net air–sea $CO_2$ flux (mol C $m^{-2}$ $yr^{-1}$; positive out of the ocean) and (b) particulate organic export at 75-m depth (mol C $m^{-2}$ $yr^{-1}$) averaged over the 1000-yr CSM 1.4-carbon control simulation.

Ocean and net invasion of $CO_2$ into the temperate and subpolar North Pacific and North Atlantic. Some differences in the spatial distribution, such as the larger net $CO_2$ efflux from the model Southern Ocean, are expected since the model represents preindustrial conditions. The patterns and integrated magnitude (8.94 ± 0.10 Pg C $yr^{-1}$) of the simulated sinking particulate organic matter export (Fig. 7b) are also generally consistent with the more limited observational constraints on this quantity (Doney et al. 2003), except for the equatorial Pacific problems already mentioned. So, too, are the water column DIC and nutrient distributions, which are governed by a combination of air–sea ex-

change, biological uptake and export, subsurface remineralization, and ocean circulation.

### e. Atmospheric $CO_2$ distributions

The time–space distribution of atmospheric $CO_2$ integrates land and ocean fluxes on regional to global scales. Because our model tracks the 3D atmospheric $CO_2$ tracer field, we can utilize the model atmospheric $CO_2$ field to assess the skill of simulated surface fluxes. Surface $CO_2$ fluxes are reflected in spatial patterns in the mean atmospheric surface $CO_2$ distribution (lowest ~60 mb; Fig. 8a). Over land, net long-term fluxes into and out of the land biosphere are approximately zero,
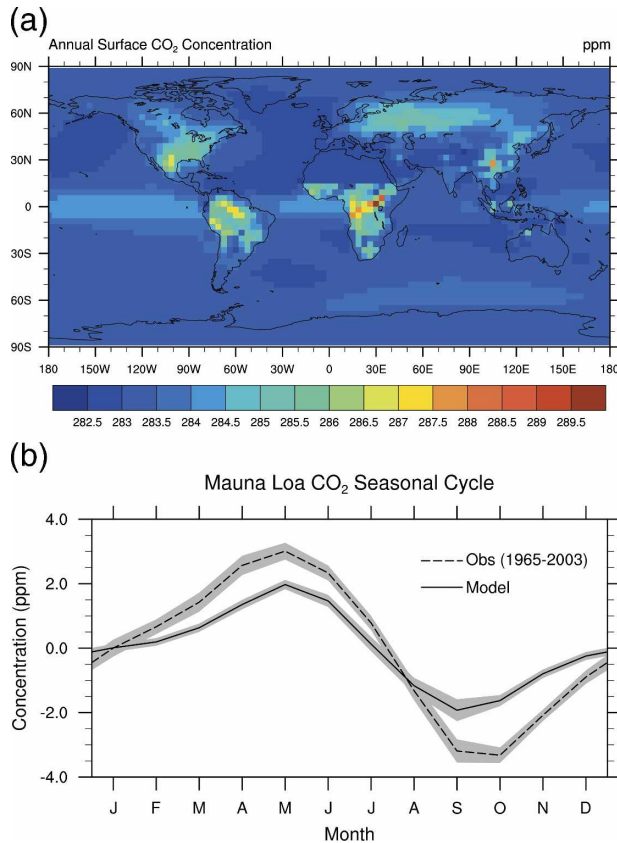
## (a)



## (b)



FIG. 8. Atmospheric surface $CO_2$ fields (ppmv) from CSM 1.4-carbon 1000-yr control simulation: (a) the mean spatial distribution averaged over the bottom two model layers ($\sim$60 mb) and (b) the mean seasonal cycle with rms interannual variability (shading) from the model and observations at the Mauna Loa Observatory. The model is sampled at the nearest sigma surface to the altitude of the Mauna Loa Observatory. Observed data are from the NOAA/Climate Monitoring and Diagnostics Laboratory.

and the elevated $CO_2$ levels found in the Tropics and Northern Hemisphere temperate zone arise from the so-called "rectifier effect" associated with seasonal correlations between surface $CO_2$ fluxes and atmospheric convection and mixing (Denning et al. 1995). Over ocean, the model exhibits a peak due to equatorial $CO_2$ outgassing regions (Fig. 7a). Atmospheric $CO_2$ is also slightly higher in the Southern Hemisphere than in the Northern Hemisphere because of the large uptake of $CO_2$ in the North Pacific and North Atlantic formation sites and subsequent southward lateral transport and release in the equatorial and Southern Oceans (Broecker and Peng 1992). The simulated mean spatial patterns in the model cannot be directly compared to modern observations, which are strongly influenced by fossil fuel emissions and fluxes due to current and past land use change.

The seasonal cycle of $CO_2$ at Mauna Loa, Hawaii,

provides a useful measure of the seasonal imbalances between NPP and $R_h$ of the Northern Hemisphere land biosphere (e.g., Fung et al. 1983; Randerson et al. 1997) and is thus an indirect constraint on the bulk turnover time of soil carbon. The 1000-yr mean $CO_2$ seasonal cycle at the location of Mauna Loa in the model resembles that observed (Fig. 8b). Both the modeled and observed cycles peak in May and have a trough in September–October; the simulated peak–trough amplitude is $\sim$4 ppmv, somewhat smaller than the observed value of $\sim$6 ppmv, which also includes the small but nonnegligible effects of seasonal transport of fossil fuel $CO_2$ (Randerson et al. 1997). The model underestimation of the $CO_2$ amplitude is also partially due to the underestimation of NPP at northern high latitudes. The agreement suggests that the seasonal dynamics of both photosynthesis and decomposition are reasonably well captured in the model, and that known deficiencies in the physical climate model have not impaired gross features of terrestrial carbon dynamics. The spatial patterns of the seasonal atmospheric $CO_2$ amplitude (not shown) are consistent with modern observations, increasing from <1–2 ppmv over the Southern Ocean to 5–15 ppmv over high-terrestrial NPP regions in the Tropics and Northern Hemisphere temperate zone. (Fig. 6a).

## 5. Natural carbon–climate variability

### a. Global surface $CO_2$ flux variability

Time series of the global integrated, annual net $CO_2$ surface fluxes from the land $\Delta F_{land}$ and ocean $\Delta F_{ocean}$ (Fig. 9) highlight the high-frequency, interannual variability in surface–atmosphere exchange. The rms variability ($1\sigma$) in the annual net global fluxes is $\pm$0.69 Pg C yr$^{-1}$ and $\pm$0.10 Pg C yr$^{-1}$, for $\Delta F_{land}$ and $\Delta F_{ocean}$, respectively. For monthly, deseasonalized anomalies, the corresponding rms variability increases to $\pm$1.40 Pg C yr$^{-1}$ and $\pm$0.19 Pg C yr$^{-1}$. As with the low-frequency signal, interannual variability in terrestrial exchange dominates over that of the ocean by almost an order of magnitude, in part because of the chemical buffering of the carbon dioxide system in seawater, with year-to-year shifts from the terrestrial biosphere as large as $\pm$2 Pg C.

The interannual variability in the simulated terrestrial flux is comparable to the value of $\pm$2.0 Pg C yr$^{-1}$ inferred from the contemporary atmospheric $CO_2$ record (Bousquet et al. 2000). Some care is required in a direct model data comparison, as the contemporary fluxes include processes [such as often human-ignited fire contributions (Langenfelds et al. 2002; Randerson et al. 2005) and variability in climate due to volcanic
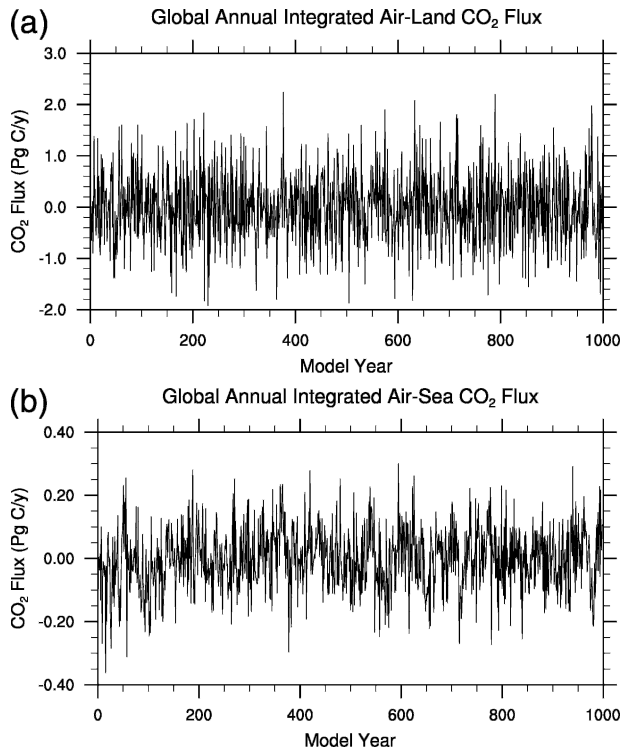
FIG. 9. Time series of global integrated, annual net (a) land and (b) ocean $CO_2$ fluxes (Pg C yr$^{-1}$) from the CSM 1.4-carbon 1000-yr control simulation, highlighting the magnitude of the interannual variability. Note the different vertical scales for (a) and (b).

eruptions and the subsequent impact on terrestrial carbon storage (Angert et al. 2004)], that are not explicitly treated in CSM 1-carbon. The modeled variability is also comparable to, albeit at the low end of, that simulated in an intercomparison of terrestrial ecosystem models (Dargaville et al. 2002). Note that the simulated pentadal variability in $\Delta F_{land}$ is similar to the inferred magnitude of the anthropogenic terrestrial carbon sink; thus, the attribution of the contemporary carbon sink to processes other than climate variability remains a statistical challenge. The simulated ocean variability is considerably smaller than that inferred from atmospheric inversions but is consistent with estimates derived from historical reconstructions using ocean-only biogeochemical models [monthly global anomalies: ±0.20 Pg C yr$^{-1}$ (Le Quere et al. 2000); ±0.23 Pg C yr$^{-1}$ (Obata and Kitamura 2003)].

### b. Spatial patterns in $CO_2$ flux variability

The geographic distribution of the rms variability in the annual means of $\Delta F_{land}$ and $\Delta F_{ocn}$ (1$\sigma$ standard deviation of the time series at each individual grid point) is shown in Fig. 10a. Variability in $\Delta F_{land}$ is largest in the Tropics, with peak values exceeding 100–200 g C

m$^{-2}$ yr$^{-1}$, and is elevated (20–100 g C m$^{-2}$ yr$^{-1}$) across temperate North America and Eurasia. The tropical variability maxima occur in bands of moderate NPP surrounding the terrestrial NPP maxima in Amazonia, Central Africa, and Indonesia (Fig. 6a). Locally, the air–sea $CO_2$ flux variability of the annual means ranges from 1 to >10 g C m$^{-2}$ yr$^{-1}$ in the coupled model, with maxima in the subpolar North Atlantic and North Pacific, Southern Ocean, and in two off-equatorial bands in the tropical Pacific. There is a general correspondence between the locations of the maxima in air–sea $CO_2$ flux variability and the regions of strong $CO_2$ uptake and degassing (Fig. 7a).

The largest variability in our air–sea flux is in the Southern Ocean and North Atlantic. This is in contrast to most modeling and observational studies that show the highest air–sea $CO_2$ flux variability to be associated with El Niño–Southern Oscillation (ENSO), accounting for the majority of the total global variability in ocean-only simulations [70%, (Le Quere et al. 2000); >50% (Obata and Kitamura 2003)] and coupled ocean–atmosphere simulations (e.g., Jones et al. 2001). This could be because these ocean-only models underestimate high-latitude ocean dynamics and biology. It could also be because of overly weak vertical gradients in DIC in the upper thermocline in the CSM 1.4-carbon model Tropics, caused by overly strong iron limitation and, therefore, low surface biological uptake (Fig. 7b). In contrast to the model results, equatorial Pacific observations show that the highest interannual variability in air–sea $CO_2$ flux occurs on or near the equator. In the field data, it appears to be driven primarily by the shoaling and deepening of the thermocline in the central and eastern basin, which in turn alters the magnitude of subsurface inorganic carbon upwelling. The model simulations include corresponding changes in thermocline depth (20°C isotherm). The variability in simulated monthly sea surface temperature anomalies (±0.72 K) in the central equatorial Pacific in the 1000-yr control agrees well with observations (±0.82 K), suggesting that our low tropical variability is not an issue of thermocline variability or physical upwelling (Otto-Bliesner and Brady 2001). The problem appears instead to be that the vertical inorganic carbon gradients are too weak so that even with thermocline shoaling or deepening, there is insufficient variability in the inorganic carbon concentrations of the upwelled source water.

Not surprisingly, the model regions with high surface $CO_2$ flux variability create corresponding areas of elevated variability in the overlying surface atmospheric $CO_2$ field (Fig. 10b). Rms variability (1$\sigma$) in the spatial anomalies in annual surface $CO_2$ concentrations (after removal of global mean) range from <0.2 ppmv over
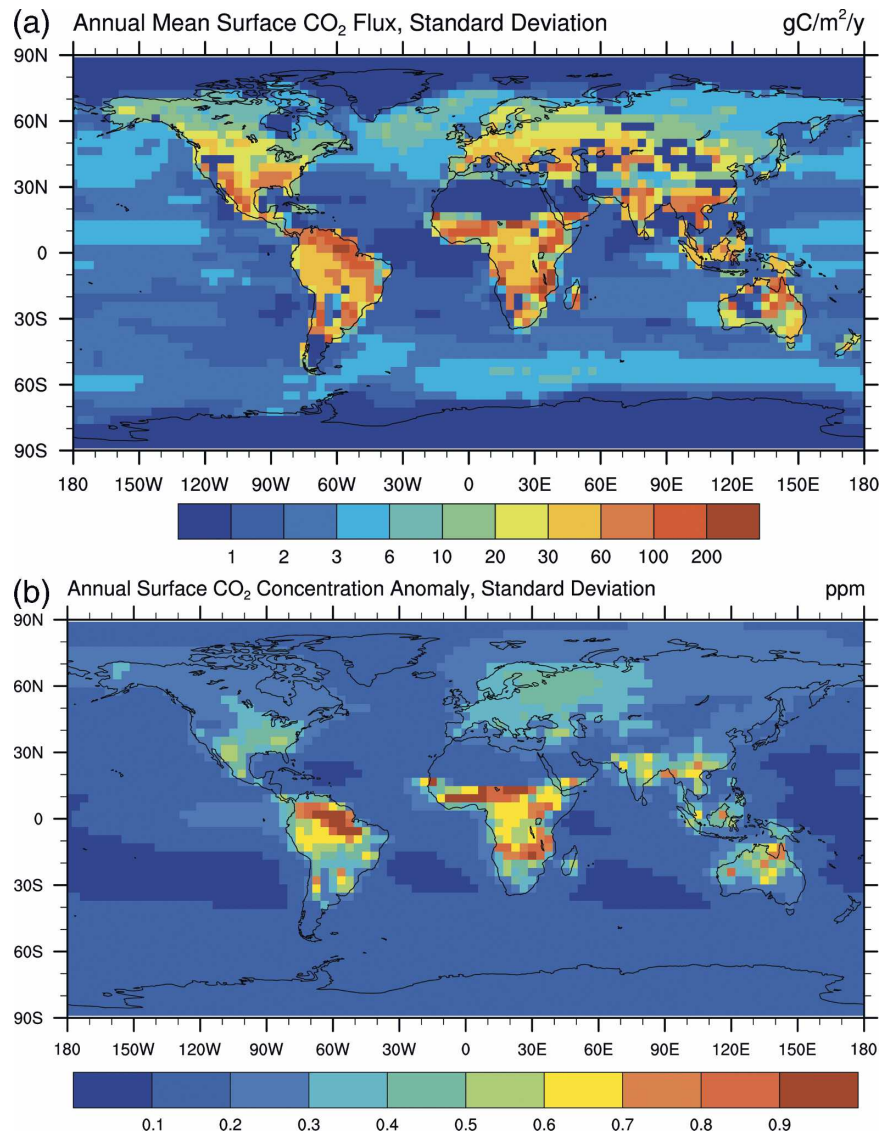
FIG. 10. Spatial maps of the rms variability ($1\sigma$) of (a) annual net surface $CO_2$ fluxes (g C m$^{-2}$ yr$^{-1}$) and (b) annual surface atmospheric $CO_2$ spatial concentration anomalies (ppmv) over the 1000-yr CSM 1.4-carbon control simulation. Note the nonlinear scale in (a).

oceans to 0.2–0.5 ppmv over northern Eurasia and eastern North America to as high as 0.5–1.0 ppmv in the Tropics. The spatial patterns in the annual mean and rms spatial variability in surface atmospheric $CO_2$ are almost identical between the cases with and without land $CO_2$ fertilization.

### c. Terrestrial variability mechanisms

Terrestrial photosynthesis and decomposition are enhanced by positive temperature and soil moisture anomalies (unless thresholds are exceeded), and the net effect on NPP and $R_h$ depends on their synergistic or competing effects. Over land, the interannual variabil-

ity of surface air temperature and soil moisture is positively correlated (warm–wet and cool–dry) when mean air temperature is low (e.g., temperate latitudes in winter and polar regions in the summer) and negatively correlated (warm–dry and cool–wet) when the mean air temperatures are high (Tropics all year and temperate bands in the summer). These distinct regional/seasonal patterns are illustrated in Fig. 11a, which is a spatial map of the air temperature–soil moisture correlation for the Northern Hemisphere summer. Interannual variations in simulated NEP tend to be controlled by summer moisture stress (annual mean stress in the case of the Tropics) rather than temperature stress (Fig.
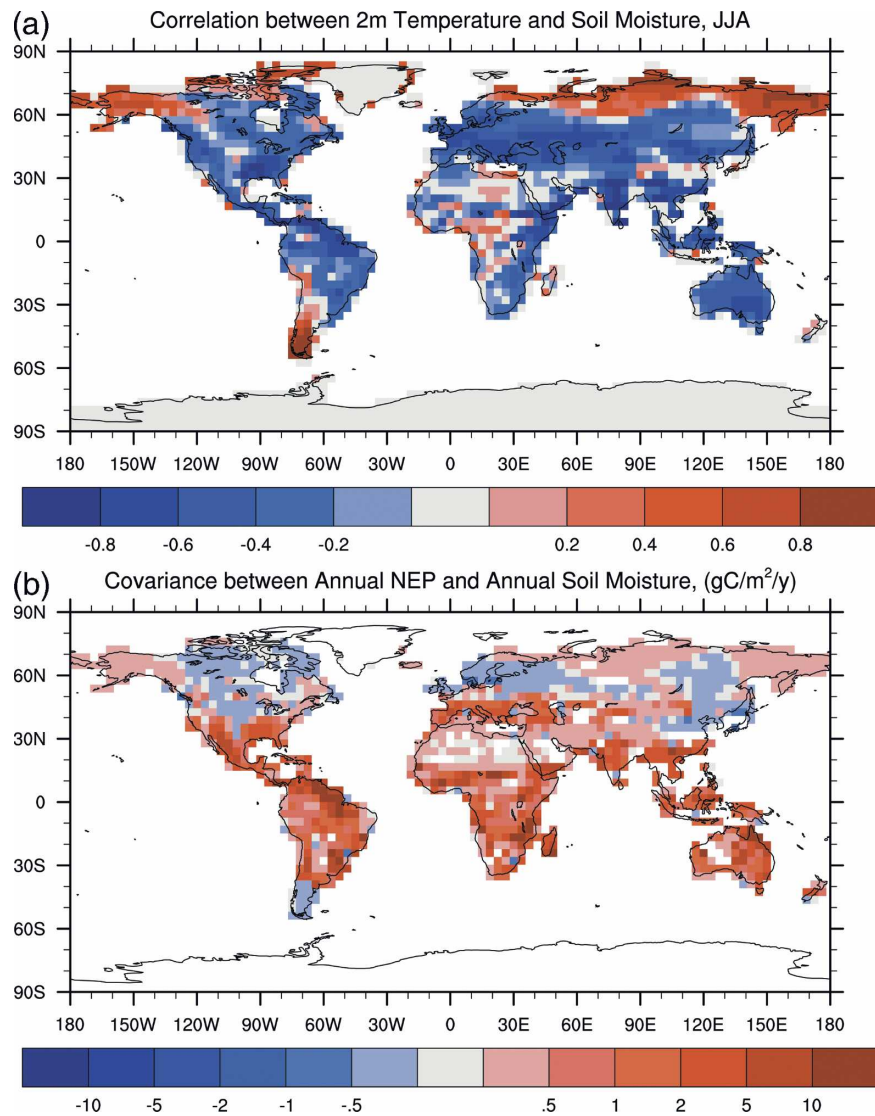
FIG. 11. Spatial maps of the (a) correlation between anomalies in surface 2-m air temperature and in soil moisture for June–August and (b) covariance of annual NEP and annual mean nondimensional model soil moisture stress term $g(w)$ [see Eq. (4)] from the CSM 1.4-carbon 1000-yr control run (gray regions are where the correlation is not significant).

11b). An exception is in the polar Northern Hemisphere, where temperature and moisture effects are synergistic and comparable in size.

Because the turnover time of vegetation carbon is shorter than that of soil carbon, NPP is slightly more sensitive to climate perturbations than $R_h$, $\pm 0.88$ Pg C yr$^{-1}$ versus $\pm 0.54$ Pg C yr$^{-1}$ ($1\sigma$ rms, global net annual mean), respectively. Thus, NPP decreases faster than $R_h$ with climate stress and increases faster than $R_h$ under favorable climate conditions (Fig. 12a). NPP and $R_h$ covary on subannual time scales. Globally, however, the linkage of land photosynthesis to respiration is con-

siderably weaker on interannual time scales because regional flux anomalies tend to cancel.

Variations in simulated terrestrial NEP can be driven by NPP, $R_h$, or both. In our model formulation, the climate modulations are the same for all the dead carbon pools [cf. Eq. (4)]. The respiratory fluxes from the fast ($\tau_k < 5$ yr) pools are in step with NPP and cancel 50%–60% of the NPP. It is the variation of wood biomass, CWD, and the "leakage" of dead carbon from the litter to the slow pool that determine NEP on decadal-to-centennial time scales. Unlike the fluxes, the variability of these pools is comparable on interannual and
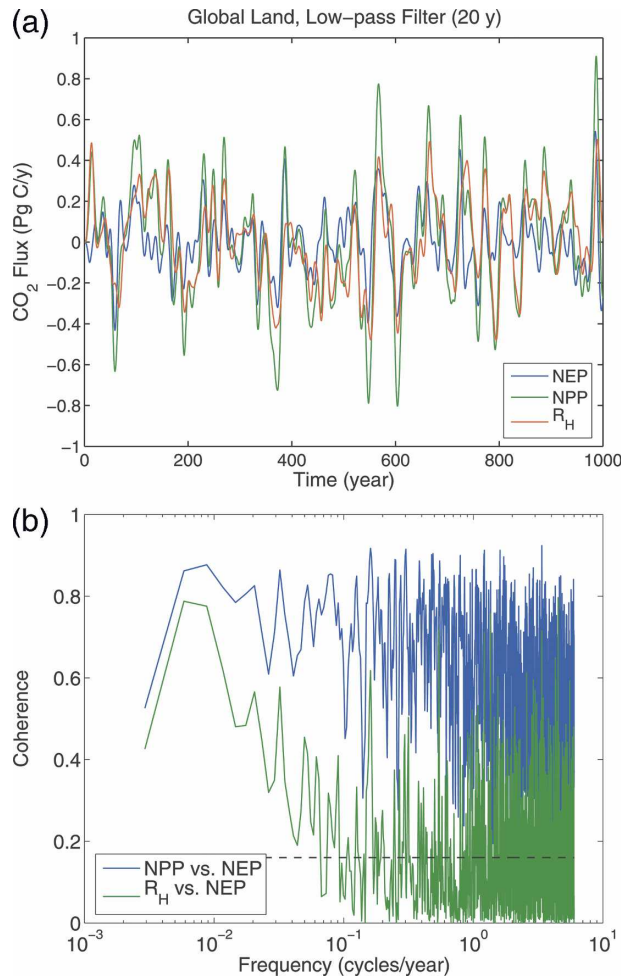
## (a)



## (b)



FIG. 12. (a) Time series of low-pass-filtered, global net land NPP, $R_h$, and NEP (Pg C yr$^{-1}$) from the CSM 1.4-carbon 1000-yr control simulation. A 20-yr Hanning filter is used to remove high-frequency variability. (b) The squared coherence (0–1) vs frequency (cpy) from cross-spectrum analyses of global land NEP vs NPP and $R_h$.

interdecadal time scales (Fig. 4c), with $1\sigma$ rms for global annual means of $\pm 1.51$, $\pm 0.63$, and $\pm 0.95$ Pg C for wood, CWD, and the slow pool, respectively. Figure 12b shows squared coherence versus frequency for NEP against NPP and NEP against $R_h$; the squared coherence varies from 0 (completely incoherent or uncorrelated at all phase lags) to 1 (fully coherent) and indicates the fraction of variance that can be accounted for between the two time series with a linear model. NEP, the noncancellation between NPP and $R_h$, is essentially uncorrelated with $R_h$ on all time scales shorter than 10 yr. But $R_h$ is coherent with both NPP and NEP on centennial time scales, lagging by about a decade (turnover time of CWD), and largely tracks the variations in net accumulation–loss of soil/detrital carbon [cf. Eq. (3)].

### d. Ocean variability mechanisms

Several competing mechanisms govern oceanic $CO_2$ flux variability in the 1000-yr control, and the relative magnitudes (and even the signs) of the interactions differ from region to region and by time scale. The variability in net air–sea $CO_2$ flux $\Delta F_{ocn}$ (Fig. 10a) can be analyzed in terms of the components contributing to the model air–sea flux parameterization [Eq. (5)]. The transfer velocity $k_u$ depends on the square of 10-m wind speed $U^2$. Wind-driven variability contributes to high-frequency flux variability everywhere, with the sign of the $U^2$–$\Delta F_{ocn}$ correlation depending on mean net air–sea flux patterns (Fig. 7a). Sea ice coverage plays a role at high latitude both in terms of capping gas exchange and altering stratification. The impact of low-frequency variations in pCO$_2^{atm}$ on $\Delta F_{ocn}$ is discussed in section 5e; the high-frequency atmospheric signal is small enough over the ocean (Fig. 10b) to have little impact on air–sea flux.

Variability in surface water pCO$_2^{sw}$ is governed by thermal solubility and freshwater inputs (cooling and freshening decrease pCO$_2$), biological uptake and particle export that draw down DIC and alkalinity with the net effect of reducing pCO$_2$, and mixing/circulation that can bring up subsurface waters with elevated DIC, alkalinity, nutrients, and pCO$_2$ (metabolic $CO_2$) due to respiration of organic matter at depth. The interplay of these different factors is shown in a set of $\Delta F_{ocn}$ versus property covariance maps (Fig. 13). Interannual variations in freshwater fluxes associated with the model ENSO lead to surface freshening, warming, stratification, and negative $CO_2$ flux anomalies (uptake), driving the large off-equator variability in the tropical Indo-Pacific (Fig. 10a). Net freshwater input to the surface ocean lowers sea surface salinity (SSS), reducing both DIC and alkalinity by dilution. The thermodynamics of the ocean carbonate system is such that dilution (negative SSS anomaly) lowers surface water pCO$_2$ and drives a downward (negative) $CO_2$ flux anomaly, which accounts for the large positive SSS–$CO_2$ flux covariance in Fig. 13c. Note that the SST–$CO_2$ flux covariance in these regions is negative, opposite that of thermodynamics (warming leading to increased seawater pCO$_2$), and demonstrates that haline forcing dominates over thermal.

The effects of particle export and circulation are often opposed to each other because the same enhanced mixing or upwelling that brings nutrients to the surface to enhance production (lower pCO$_2$ and positive, downward ocean $CO_2$ uptake anomaly) also brings DIC that increases pCO$_2$. In the deep-mixing zones of the Southern Ocean and North Atlantic, upwelled DIC

(a)

Covariance of Air-Sea $CO_2$ Flux and MLD, (mol C/m$^2$/y)(m)

(b)

Covariance of Air-Sea $CO_2$ Flux and SST, (mol C/m$^2$/y)(C)

(c)

Covariance of Air-Sea $CO_2$ Flux and SSS, (mol C/m$^2$/y)(psu)

(d)

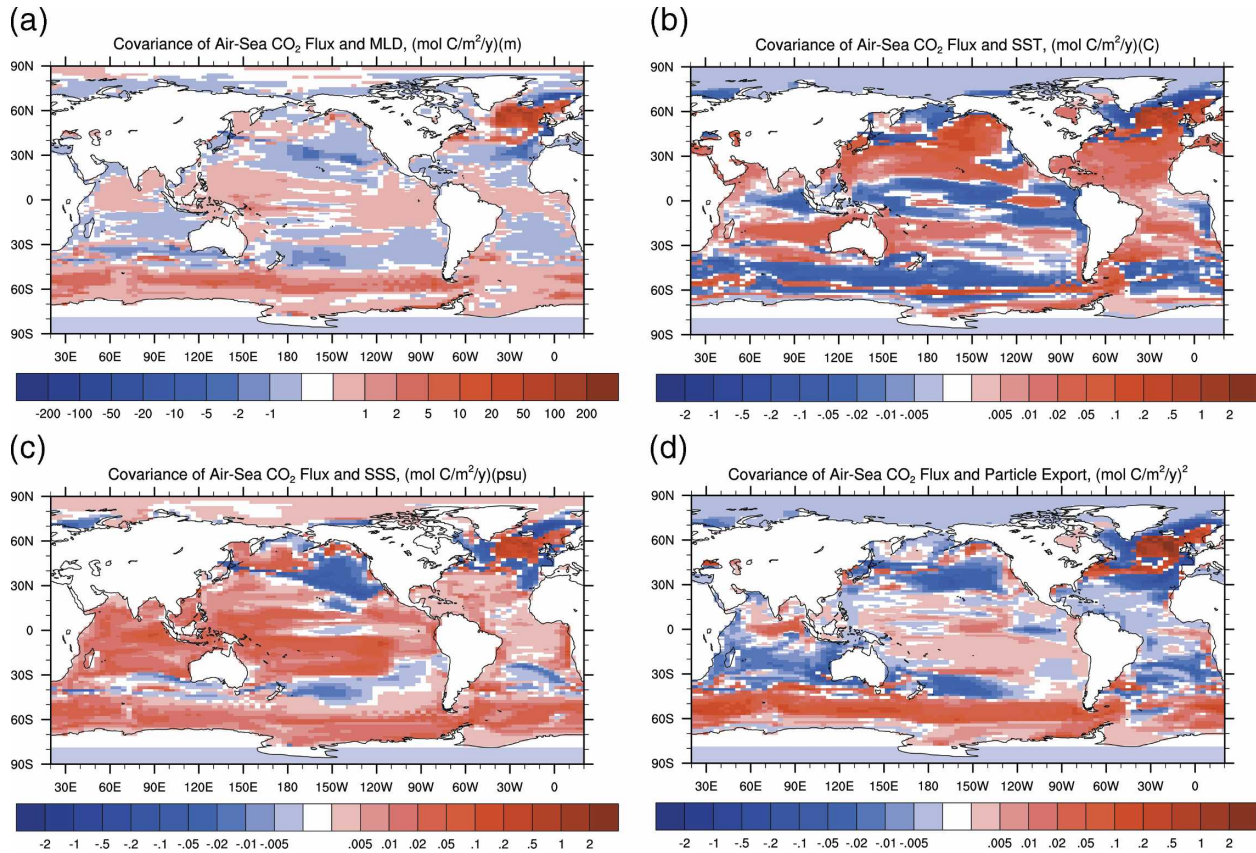Covariance of Air-Sea $CO_2$ Flux and Particle Export, (mol C/m$^2$/y)$^2$

FIG. 13. Spatial covariance maps of annual mean air–sea $CO_2$ flux (positive out of the ocean) and biological and physical forcing factors including (a) mixed layer depth, (b) SST, (c) SSS, and (d) export production.

from deeper mixing overwhelms enhanced biological drawdown, leading to positive $CO_2$ flux anomalies (outgassing). In the Southern Ocean, deeper mixing is associated with colder SSTs, while the opposite pattern occurs in the subpolar North Atlantic, where mixing is governed by sea ice distributions and surface salinity.

### e. Ocean damping of land-driven atmospheric $CO_2$ variability

The power spectral densities (Pg C yr$^{-1}$)$^2$ cpy$^{-1}$ in the simulated global net land and ocean $CO_2$ fluxes are plotted in Fig. 14a versus the log of frequency (cpy). The spectral analysis utilizes monthly, deseasonalized anomalies where a mean seasonal climatology has been removed from the global time series of $\Delta F_{\text{land}}$ and $\Delta F_{\text{ocean}}$. Figure 14b displays the spectrum for the total flux (land + ocean) but it is plotted in a variance-preserving form where the area under any frequency band is proportional to variance in that band (Emery and Thomson 1998). The spectral analysis illustrates several features: terrestrial variability dominates over ocean variability at all frequencies; the spectra are white on time scales beyond a few years and thus,

most of the variance is concentrated at high frequencies (frequency >0.25 cpy; time scale <4 yr); and on a relative basis, the ocean has more variability than the land at low frequencies (frequency <0.1 cycles yr$^{-1}$; time scale >10 yr).

A cross-spectral analysis of the model global net ocean and land $CO_2$ fluxes is presented in Fig. 15. The first panel displays the squared coherence versus frequency; squared coherence varies from 0 (completely incoherent or uncorrelated at all phase lags) to 1 (fully coherent) and indicates the fraction of variance that can be accounted for between the two time series with a linear model. The average coherence of $\Delta F_{\text{land}}$ and $\Delta F_{\text{ocean}}$ on the subannual time scale is low, essentially indistinguishable from zero at the 95% confidence level. The global time series are strongly coherent on time scales of 2–100 yr, and the land $CO_2$ fluxes can explain 40%–90% of the variance in the ocean fluxes.

The mechanism and relationship between $\Delta F_{\text{land}}$ and $\Delta F_{\text{ocean}}$ vary with time scale. The second panel (Fig. 15b) displays the phase difference (in degrees) between $\Delta F_{\text{land}}$ and $\Delta F_{\text{ocean}}$ (solid line) and $\Delta F_{\text{ocean}}$ and atmo-

(a)



(b)
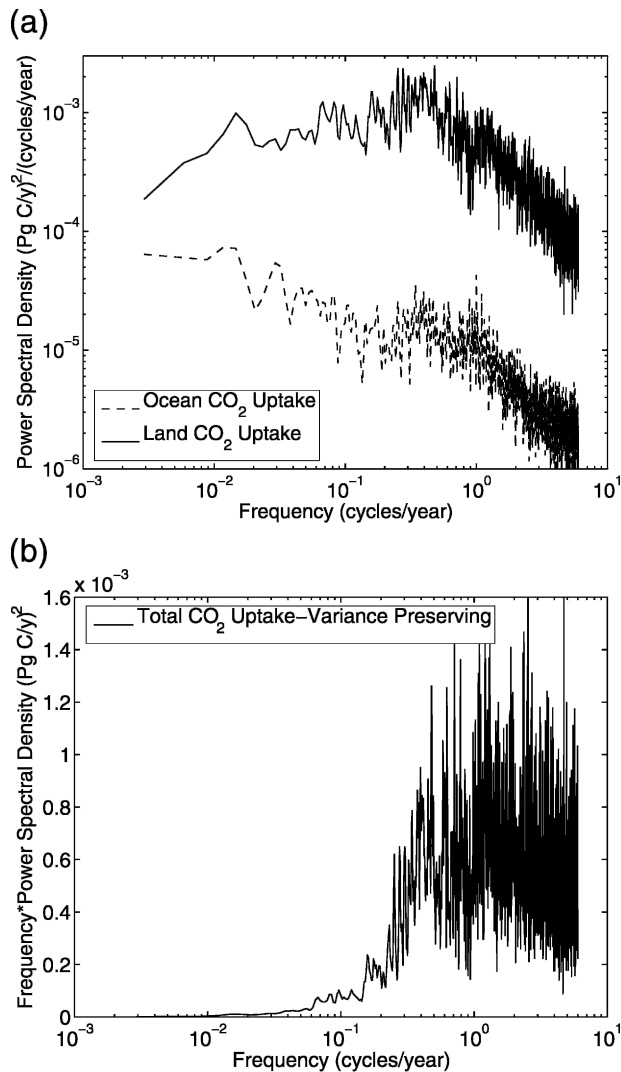


FIG. 14. (a) Power spectral density (Pg C yr$^{-1}$)$^2$ cpy$^{-1}$ vs frequency (cpy) for the global integrated land and ocean CO$_2$ fluxes from the CSM 1.4-carbon 1000-yr control simulation. The power spectra are for monthly anomalies generated by removing a mean seasonal cycle. (b) The spectrum for the total flux (land + ocean) in variance preserving form (frequency × power spectral density).

(a)



(b)



FIG. 15. Cross-spectrum analysis for global integrated land and ocean CO$_2$ fluxes ($\Delta F_{land}$ vs $\Delta F_{ocean}$) from CSM 1.4-carbon 1000-yr control simulation: (a) the squared coherence (0–1) vs frequency (cpy) and (b) the phase difference (degrees; <0 ocean lags) between ocean and land CO$_2$ fluxes (solid line) and ocean CO$_2$ flux and atmospheric CO$_2$ (circles). A value of 0° occurs when the time series are perfectly correlated and +/−180° when they are perfectly anticorrelated. Phase in degrees can be converted to lags/leads in years by dividing by (360° cycle$^{-1}$) × frequency (cpy). Phases are not displayed for frequencies >0.5 cpy because the $\Delta F_{land}$ vs $\Delta F_{ocean}$ coherences in (a), on average, are equivalent to 0 at the 95% confidence level.

spheric CO$_2$ inventory (circles) as a function of frequency. Assuming that the pairs of time series are coherent (Fig. 15a), a phase of 0° occurs when the time series are perfectly correlated (peaks matching peaks) and +/−180° when perfectly anticorrelated (peaks matching troughs). Negative phases mean the ocean lags either the land fluxes or atmosphere CO$_2$. On time scales of a few years (frequency 0.25–0.50 cycles yr$^{-1}$), the ocean and land fluxes are approximately in phase (~+50°), with the ocean somewhat leading the land by a few months. Although the land and ocean CO$_2$ fluxes partially amplify each other with respect to their im-
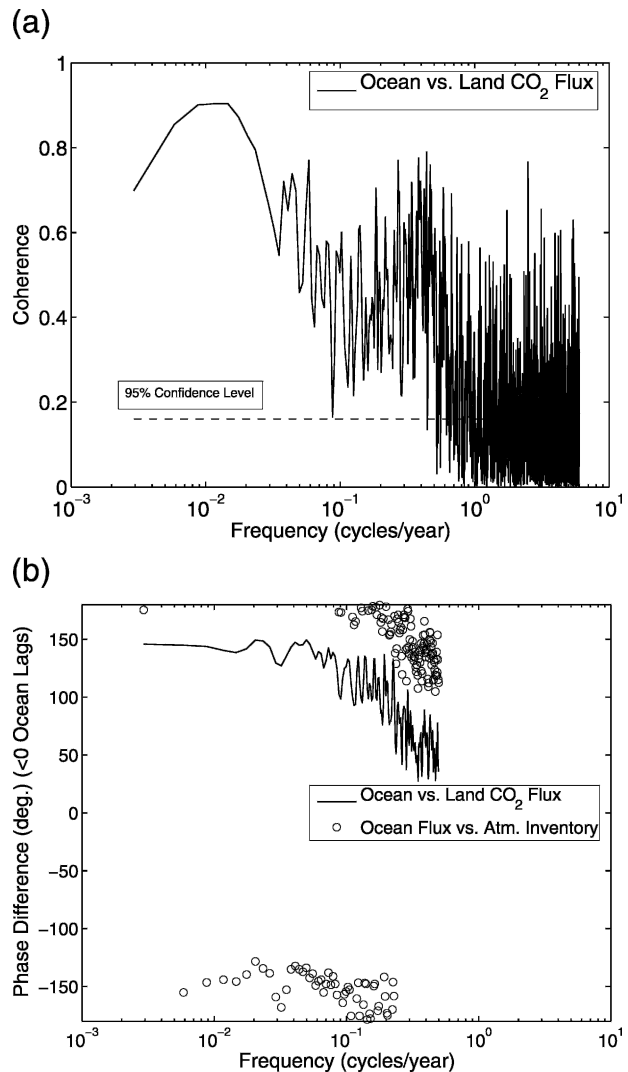
pacts on atmospheric CO$_2$, the two carbon reservoirs are only indirectly coupled via the biogeochemical responses to regional and global physical climate modes [ENSO, North Atlantic Oscillation (NAO), etc.; Wang and Schimel (2003)].

The small positive ocean–land phase difference in the model is somewhat counter to the expectation based on

ENSO observations. During an El Niño, negative ocean $CO_2$ flux anomalies (reduced outgassing) arise in the equatorial Pacific a few months prior to the larger positive terrestrial flux anomalies (e.g., Jones et al. 2001). The along-equator upwelling-driven interannual variability in our model simulations is too small and the different land–ocean interannual variability phasing is governed by the ENSO response of the off-equator variability bands (salinity forcing) and model ENSO teleconnections on temperate ocean biogeochemistry variability.

On decadal and longer time scales, $\Delta F_{land}$ and $\Delta F_{ocean}$ are closer to being anticorrelated (Fig. 15b), and the land–ocean carbon coupling occurs more directly through variations in atmospheric $CO_2$. At a phase of $+180°$, the troughs in ocean $CO_2$ flux would exactly line up with the peaks in the land flux (and vice versa); since the land–ocean phase difference is $\sim+150°$, the ocean troughs somewhat lag the land peaks by $\sim1$ to 10 yr on decadal-to-centennial time scales, respectively. Correspondingly, the ocean troughs somewhat lead the atmospheric $CO_2$ peaks by a roughly similar amount of time. The strong land–ocean coherence (Fig. 15a) and phasing (Fig. 15b) suggest that global low-frequency carbon cycle variability originates on the land and then propagates into the atmosphere and ocean. For example, a $CO_2$ release from the terrestrial biosphere results in the growth of atmospheric $CO_2$ that in turn drives a net air–sea $CO_2$ flux into the ocean; the maximum ocean uptake occurs prior to the peak in atmospheric concentrations when the temporal gradient is largest (Fig. 16). The strength of this ocean damping of land-induced atmospheric $CO_2$ variability is about 20%–25% on multidecadal scales.

Direct comparison of the estimated multidecadal to centennial variability from CSM 1-carbon against contemporary observations is complicated by the limited temporal duration of data records (a few decades at most) together with the large impacts of anthropogenic activities on the carbon cycle (including fossil fuel emissions, land use, and climate change). For the preindustrial period, perhaps the best datasets with sufficient time resolution and global scale are atmospheric $CO_2$ time series from bubbles trapped in high-deposition ice cores [e.g., Law Dome (Etheridge et al. 1996), Taylor Dome (Indermühle et al. 1999), and Dronning Maud Land (Siegenthaler et al. 2005)]. The simulated peak to peak centennial-scale variability from CSM 1.4-carbon ($\sim5$ ppmv $CO_2$) is comparable to that from ice core records (e.g., $\sim6$ ppmv $CO_2$; Siegenthaler et al. 2005), but the agreement may be misleading because of drift issues in the model simulations, the omission of external volcanic and solar climate–carbon perturbations
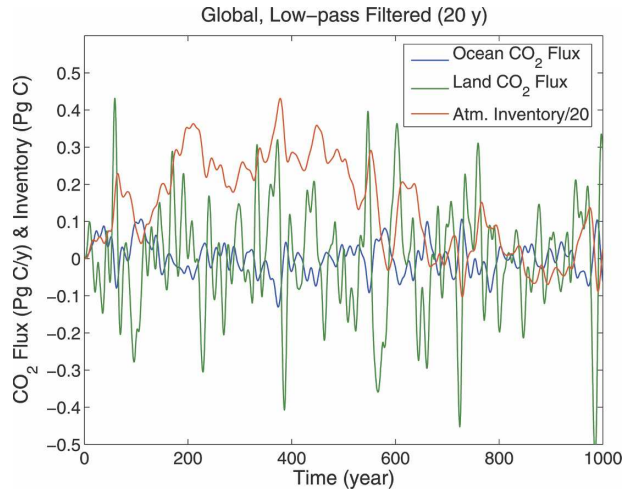


FIG. 16. Same as in Fig. 12a, but for land and ocean $CO_2$ fluxes (Pg C $yr^{-1}$) and atmospheric $CO_2$ inventory anomaly (Pg C; scaled by dividing by 20).

(Gerber et al. 2003; Trudinger et al. 2005), and possible analytical errors in the ice record. The validation problem is even more challenging on decadal scales because of limited temporal resolution and low precision for the ice core data.

## 6. Discussion

This paper documents the development of and results from the first coupled carbon–climate model in the NCAR CCSM framework. The 1000-yr integration is stable, and the simulated climatologies in carbon inventory and fluxes resemble, to the lowest order, those determined from available observations. Atmospheric $CO_2$ excursions are small, $\sim4$ ppm over several centuries, and no abrupt changes are found in this integration. Documentable discrepancies between simulations and observations can be traced to biases in the physical climate in the model, so that future development of the carbon modules must be accompanied by concomitant improvements in the climate models.

Analysis of the 1000-yr integration shows that globally terrestrial fluxes are more variable than oceanic fluxes on all time scales; however, different processes dominate the variability on different time scales. Variability of the land fluxes and ocean fluxes on interannual time scales is principally a response to interannual variability in surface climate, and so these fluxes are, to the lowest order, independent of one another, even though they both have statistics similar to climate variability. Long time-scale ($10^1$–$10^2$ yr) variability of land fluxes is modulated by the slowly decomposing coarse woody debris and soil carbon pools, while that of the

ocean fluxes is modulated by variability of atmospheric $CO_2$. It is on decadal and longer time scales that the atmosphere–land–ocean coupling becomes evident. Climate variability drives changes in the land NEP. This in turn alters atmospheric $CO_2$ and drives changes in the air–sea exchange of $CO_2$. The reverse does not happen in our 1000-yr simulation, as the variability in the ocean fluxes is too small to drive an atmospheric $CO_2$ anomaly (and concomitant climate anomaly) that could impact stomatal conductance on land.

The variability of the land and ocean fluxes is the "noise" in the detection of anthropogenic carbon sinks. Short-term NEP is driven by changes in NPP, which is more sensitive than $R_h$ to climate perturbations. The detrital and soil carbon pools are minor contributors to the instantaneous $R_h$ variability, and their slow variations set the background for long-term NEP. Thus, not only is the variability in terrestrial NEP comparable in magnitude to the contemporary land sink for anthropogenic $CO_2$, but also, inferences about NEP processes based on interannual variability may not hold on longer time scales.

Our coupled simulations highlight the need for the improved understanding of the linkages between the terrestrial carbon and water cycles on seasonal-to-decadal time scales. Water and carbon storage are intimately coupled in the CCSM simulations, with interannual variability in carbon storage primarily reflecting regional reductions in net primary production modulated by periods of elevated moisture stress. In Fung et al. (2005), we find that similar mechanisms, namely, regional soil moisture dependence, control the simulated responses of net ecosystem exchange to anthropogenic climate change; drier conditions in the Tropics lead to the destabilization of carbon inventories and $CO_2$ venting to the atmosphere while warmer and wetter conditions in temperate to high latitudes lead to enhanced carbon storage. There is a growing body of observational evidence that large-scale patterns in terrestrial productivity and carbon cycle dynamics at mid- and high latitudes in the Northern Hemisphere are driven by drought (Angert et al. 2005; Ciais et al. 2005).

## REFERENCES

Angert, A., S. Biraud, C. Bonfils, W. Buermann, and I. Fung, 2004: $CO_2$ seasonality indicates origins of post-Pinatubo sink. *Geophys. Res. Lett.,* **31,** L11103, doi:10.1029/2004GL019760.

——, ——, ——, C. C. Henning, W. Buermann, J. Pinzon, C. J. Tucker, and I. Fung, 2005: Drier summers cancel out the $CO_2$ uptake enhancement induced by warmer springs. *Proc. Natl. Acad. Sci. USA,* **102,** doi:10.1073/pnas.0501647102.

Archer, D. E., and K. Johnson, 2000: A model of the iron cycle in the ocean. *Global Biogeochem. Cycles,* **14,** 269–280.

Bacastow, E., and E. Maier-Reimer, 1990: Ocean-circulation model of the carbon cycle. *Climate Dyn.,* **4,** 95–125.

Blackmon, M., and Coauthors, 2001: The Community Climate System Model. *Bull. Amer. Meteor. Soc.,* **82,** 2357–2376.

Bonan, G. B., 1996: The NCAR Land Surface Model (LSM version 1.0) coupled to the NCAR Community Climate Model. NCAR Tech. Note NCAR/TN-429+STR, 171 pp.

Bousquet, P., P. Peylin, P. Ciais, C. Le Quere, P. Friedlingstein, and P. P. Tans, 2000: Regional changes in carbon dioxide fluxes of land and oceans since 1980. *Science,* **290,** 1342–1346.

Boville, B. A., and P. R. Gent, 1998: The NCAR Climate System Model, version one. *J. Climate,* **11,** 1115–1130.

——, J. T. Kiehl, P. J. Rasch, and F. O. Bryan, 2001: Improvements to the NCAR CSM-1 for transient climate simulations. *J. Climate,* **14,** 164–179.

Broecker, W. S., and T.-H. Peng, 1992: Interhemispheric transport of carbon dioxide by ocean circulation. *Nature,* **356,** 587–589.

Ciais, P., and Coauthors, 2005: Europe-wide reduction in primary productivity caused by the heat and drought in 2003. *Nature,* **437,** 529–533.

Collatz, G. J., J. A. Berry, G. D. Farquhar, and J. Pierce, 1990: The relationship between the Rubisco reaction mechanism and models of leaf photosynthesis. *Plant Cell Environ.,* **13,** 219–225.

Cox, P. M., R. A. Betts, C. D. Jones, S. A. Spall, and I. J. Totterdell, 2000: Acceleration of global warming due to carbon cycle feedbacks in a coupled climate model. *Nature,* **408,** 184–187.

Cramer, W., and Coauthors, 2001: Global response of terrestrial ecosystem structure and function to CO2 and climate change: Results from six dynamic global vegetation models. *Global Change Biol.,* **7,** 357–373.

Dai, A., T. M. L. Wigley, B. A. Boville, J. T. Kiehl, and L. E. Buja, 2001: Climates of the twentieth and twenty-first centuries simulated by the NCAR Climate System Model. *J. Climate,* **14,** 485–519.

Danabasoglu, G., J. C. McWilliams, and W. G. Large, 1996: Approach to equilibrium in accelerated ocean models. *J. Climate,* **9,** 1092–1110.

Dargaville R. J., and Coauthors, 2002: Evaluation of terrestrial carbon cycle models with atmospheric $CO_2$ measurements: Results from transient simulations considering increasing $CO_2$, climate, and land-use effects. *Global Biogeochem. Cycles,* **16,** 1092, doi:10.1029/2001GB001426.

Denning, A. S., I. Fung, and D. Randall, 1995: Strong simulated meridional gradient of atmospheric $CO_2$ due to seasonal exchange with the terrestrial biota. *Nature,* **376,** 240–242.

Dickinson, R. E., M. Shaikh, R. Bryant, and L. Graumlich, 1998: Interactive canopies for a climate model. *J. Climate,* **11,** 2823–2836.

Doney, S. C., K. Lindsay, and J. K. Moore, 2003: Global ocean carbon cycle modeling. *Ocean Biogeochemistry: The Role of the Ocean Carbon Cycle in Global Change,* M. J. R. Fasham, Ed., Springer-Verlag, 217–238.

——, and Coauthors, 2004: Evaluating global ocean carbon models: The importance of realistic physics. *Global Biogeochem. Cycles,* **18,** GB3017, doi:10.1029/2003GB002150.

Dufresne, J.-L., P. Friedlingstein, M. Berthelot, L. Bopp, P. Ciais, L. Fairhead, H. Le Treut, and P. Monfray, 2002: On the magnitude of positive feedback between future climate change and the carbon cycle. *Geophys. Res. Lett.,* **29,** 1405, doi:10.1029/2001GL013777.

Emery, W. J., and R. E. Thomson, 1998: *Data Analysis Methods in Physical Oceanography.* Pergamon, 634 pp.

Etheridge, D. M., L. P. Steele, R. L. Langenfelds, R. J. Francey, J.-M. Barnola, and V. I. Morgan, 1996: Natural and anthropogenic changes in atmospheric $CO_2$ over the last 1000 years from air in Antarctic ice and firn. *J. Geophys. Res.,* **101D,** 4115–4128.

Friedlingstein, P., G. Joel, C. B. Field, and I. Y. Fung, 1999: Toward an allocation scheme for global terrestrial carbon models. *Global Change Biol.,* **5,** 755–770.

——, L. Bopp, P. Ciais, J. Dufresne, L. Fairhead, H. LeTreut, P. Monfray, and J. Orr, 2001: Positive feedback between future climate change and the carbon cycle. *Geophys. Res. Lett.,* **28,** 1543–1546.

——, and Coauthors, 2006: Climate–carbon cycle feedback analysis: Results from the C4MIP model intercomparison. *J. Climate,* **19,** 3337–3353.

Fung, I., K. Prentice, E. Matthews, J. Lerner, and G. Russell, 1983: Three-dimensional tracer model study of atmospheric $CO_2$: Response to seasonal exchange with the terrestrial biosphere. *J. Geophys. Res.,* **88** (C2), 1281–1294.

——, S. C. Doney, K. Lindsay, and J. John, 2005: Evolution of carbon sinks in a changing climate. *Proc. Natl. Acad. Sci. USA,* **102,** doi:10.1073/pnas.0504949102.

Gerber, S., F. Joos, P. Brügger, T. F. Stocker, M. E. Mann, S. Stich, and M. Scholze, 2003: Constraining temperature variations over the last millennium by comparing simulated and observed atmospheric $CO_2$. *Climate Dyn.,* **20,** 281–299.

Govindasamy, B., S. Thompson, A. Mirin, M. Wickett, K. Caldeira, and C. Delire, 2005: Increase of carbon cycle feedback with climate sensitivity: Results from a coupled climate and carbon cycle model. *Tellus,* **57B,** 153–163.

Hansen, J. E., M. Sato, A. Lacis, and V. Oinas, 1998: Climate forcings in the industrial era. *Proc. Natl. Acad. Sci. USA,* **95,** 12 753–12 758.

Houghton, J. T., Y. Ding, D. J. Griggs, M. Noguer, P. J. van der Linden, X. Dai, K. Maskell, and C. A. Johnson, Eds., 2001: *Climate Change 2001: The Scientific Basis.* Cambridge University Press, 881 pp.

Indermühle, A., and Coauthors, 1999: Holocene carbon-cycle dynamics based on $CO_2$ trapped in ice at Taylor Dome, Antarctica. *Nature,* **398,** 121–126.

Jones, C. D., M. Collins, P. M. Cox, and S. A. Spall, 2001: The carbon cycle response to ENSO: A coupled climate–carbon cycle model study. *J. Climate,* **14,** 4113–4129.

Langenfelds, R. L., R. J. Francey, B. C. Pak, L. P. Steele, J. Lloyd, C. M. Trudinger, and C. E. Allison, 2002: Interannual growth rate variations of atmospheric $CO_2$ and its $\delta^{13}C$, $H_2$, $CH_4$, and CO between 1992 and 1999 linked to biomass burning. *Global Biogeochem. Cycles,* **16,** 1048, doi:10.1029/2001GB001466.

Le Quere, C., J. C. Orr, P. Monfray, and O. Aumont, 2000: Interannual variability of the oceanic sink of $CO_2$ from 1979 through 1997. *Global Biogeochem. Cycles,* **14,** 1247–1265.

Mahowald, N., C. Luo, J. del Corral, and C. S. Zender, 2003: Interannual variability in atmospheric mineral aerosols from a 22-year model simulation and observational data. *J. Geophys. Res.,* **108,** 4352, doi:10.1029/2002JD002821.

Maier-Reimer, E., 1993: Geochemical cycles in an ocean general circulation model: Preindustrial tracer distributions. *Global Biogeochem. Cycles,* **7,** 645–677.

Mathews, H. D., A. J. Weaver, and K. J. Meissner, 2005: Terrestrial carbon cycle dynamics under recent and future climate change. *J. Climate,* **18,** 1609–1628.

Najjar, R. G., J. L. Sarmiento, and J. R. Toggweiler, 1992: Downward transport and fate of organic matter in the ocean: Simulations with a general circulation model. *Global Biogeochem. Cycles,* **6,** 45–76.

Obata, A., and Y. Kitamura, 2003: Interannual variability of air–sea exchange of $CO_2$ from 1961 to 1998 simulated with a global ocean circulation-biogeochemistry model. *J. Geophys. Res.,* **108,** 3337, doi:10.1029/2001JC001088.

Otto-Bliesner, B. L., and E. C. Brady, 2001: Tropical Pacific variability in the NCAR Climate System Model. *J. Climate,* **14,** 3587–3601.

Pearson, P. N., and M. R. Palmer, 2000: Atmospheric carbon dioxide concentrations over the past 60 million years. *Nature,* **406,** 695–699.

Petit, J. R., and Coauthors, 1999: Climate and atmospheric history of the past 420, 000 years from the Vostok ice core, Antarctica. *Nature,* **399,** 429–436.

Prentice, I. C., and Coauthors, 2001: The carbon cycle and atmospheric carbon dioxide. *Climate Change 2001: The Scientific Basis,* J. T. Houghton et al., Eds., Cambridge University Press, 183–237.

Randerson, J. T., M. V. Thompson, T. J. Conway, I. Y. Fung, and C. B. Field, 1997: The contribution of terrestrial sources and sinks to trends in the seasonal cycle of atmospheric carbon dioxide. *Global Biogeochem. Cycles,* **11,** 535–560.

——, and Coauthors, 2005: Fire emissions from $C_3$ and $C_4$ vegetation and their influence on interannual variability of atmospheric $CO_2$ and $\delta^{13}CO_2$. *Global Biogeochem. Cycles,* **19,** GB2019, doi:10.1029/2004GB002366.

Reichstein, M., and Coauthors, 2005: On the separation of net ecosystem exchange into assimilation and ecosystem respiration: Review and improved algorithm. *Global Change Biol.,* **11,** 1424–1439.

Sellers, P. J., and Coauthors, 1996: A revised land surface parameterization (SiB2) for atmospheric GCMs. Part I: Model formulation. *J. Climate,* **9,** 676–705.

Siegenthaler, U., and Coauthors, 2005: Supporting evidence from the EPICA Dronning Maud Land ice core for atmospheric $CO_2$ changes during the past millennium. *Tellus,* **57B,** 51–57.

Takahashi, T., and Coauthors, 2002: Global sea–air $CO_2$ flux based on climatological surface ocean $pCO_2$, and seasonal biological and temperature effects. *Deep-Sea Res.,* **49B,** 1601–1622.

Thompson, S. L., B. Govindasamy, A. Mirin, K. Caldeira, C. De-
lire, J. Milovich, M. Wickett, and D. Erickson, 2004: Quan-
tifying the effects of CO2-fertilized vegetation on future glob-
al climate and carbon dynamics. *Geophys. Res. Lett.,* **31,**
L23211, doi:10.1029/2004GL021239.

Trudinger, C., I. Enting, D. Etheridge, R. Francey, and P. Rayner,
2005: The carbon cycle over the past 1000 years inferred from
the inversion of ice core data. *A History of Atmospheric CO₂
and Its Effect on Plants, Animals, and Ecosystems,* J. R.
Ehleringer, T. E. Cerling, and M. D. Dearing, Eds., Ecologi-
cal Studies, Vol. 177, Springer, 329–349.

Tucker, C. J., J. E. Pinzon, M. E. Brown, D. Slayback, E. W. Pak,
R. Mahoney, E. Vermote, and N. El Saleous, 2005: An
extended AVHRR 8-km NDVI data set compatible with
MODIS and SPOT vegetation NDVI data. *Int. J. Remote
Sens.,* **26,** 4485–4498.

Wang, G., and D. Schimel, 2003: Climate change, climate modes,
and climate impacts. *Annu. Rev. Environ. Resour.,* **28,** 1–28.

Waring, R. H., J. L. Landsberg, and M. Williams, 1998: Net pri-
mary production of forests: A constant fraction of gross pri-
mary production? *Tree Physiol.,* **18,** 129–134.

Wohlfahrt, G., M. Bahn, A. Haslwanter, C. Newesely, and A.
Cernusca, 2005: Estimation of daytime ecosystem respiration
to determine gross primary production of a mountain
meadow. *Agric. For. Meteor.,* **130** (1–2), 13–25.

Zeng, N., H. Qian, E. Munoz, and R. Iacono, 2004: How strong is
carbon cycle-climate feedback under global warming? *Geo-
phys. Res. Lett.,* **31,** L20203, doi:10.1029/2004GL020904.